

Current Closure and Joule Heating in Data-Driven 3-D Auroral Arc Simulations

J. van Irsel¹, K. A. Lynch¹, A. Mule¹, M. D. Zettergren², J. K. Burchill³, L. J.
Lamarche⁴, D. L. Hampton⁵

¹Department of Physics and Astronomy, Dartmouth College, Hanover, NH, 03755 USA

²Physical Sciences Department, Embry-Riddle Aeronautical University, Daytona Beach, FL, 32114 USA

³Department of Physics and Astronomy, University of Calgary, Calgary, AB, T2N1N4 Canada

⁴SRI International, Menlo Park, CA, 94025 USA

⁵Geophysical Institute, University of Alaska Fairbanks, Fairbanks, AK, 99775 USA

Key Points:

- Understanding current closure in discrete auroral arc systems requires data-driven, three-dimensional ionospheric simulations
- Large-scale convection fields play a significant role in determining auroral arc current closure morphology and associated Joule heating
- Details of precipitating electron energy distributions can significantly affect current closure and Joule heating in auroral arc systems

Corresponding author: Jules van Irsel, jules.van.irsnel.gr@dartmouth.edu

Abstract

Discrete auroral arc systems, despite many symmetries, are three-dimensional in nature, encapsulating latitude and longitude variations in precipitation and field-aligned currents combined with important altitude variations in conductivities, hence closure currents. This study presents data-driven, 3-D numerical simulations of these processes based on a coordinated campaign of heterogeneous measurements collected from the Poker Flat Research Range during a sequence of Swarm spacecraft overpasses. These measurements include field-aligned current, global-scale convection flow, and auroral emissions, which are used to create top-boundary drivers for auroral arc simulations. Six conjunctions between the spacecraft, all-sky imagers, and radars are investigated and their measurements are used to simulate auroral arcs through multiple iterations per conjunction event. We look at different estimates of the background convection flow, assumptions about the energy distributions of electron precipitation, and along-arc structures in field-aligned current, and see what effect they have on current closure and Joule heating in auroral arc systems. Across the six conjunction events, 11 comparisons of auroral arc systems are presented, covering a catalog of 17 simulations in total. These comparisons allow us to look at the sensitivity of auroral arc systems to input parameters and envelop the simulations in a qualitative confidence interval. Our results suggest that discrete aurorae should be studied in three dimensions to fully understand field-aligned current closure and, by extension, Magnetosphere-Ionosphere-Thermosphere coupling. Additionally, our results demonstrate that both large-scale convection flows and specifics about the energy distributions of auroral precipitation can significantly affect current closure and Joule heating in auroral arc systems.

Plain Language Summary

The aurora, or northern and southern lights, are embedded within a system of interacting electric and magnetic fields, and charged particles, the more energetic of which produce the lights themselves by exciting the neutral atmosphere. This brings about a three-dimensional current system and resistive heating, known as Joule heating. These currents enter and exit the atmosphere along the Earth's magnetic field, and can only close their circuit between altitudes of 80 – 150 km, where the current carriers collide with the atmosphere. This paper outlines the importance of simulating aurorae in three-dimensions, and looks at how sensitive these simulations are to various input choices by observing the resulting differences in current connectivity and Joule heating. We look at collections of measurements from six different events and simulate them multiple times with different combinations covering 17 simulations in total. This allows us to gain insight into how much confidence can be had in our auroral arc simulations, and, by extension, what aspects are important to get right when studying auroral arcs. We conclude that large-scale plasma motion and the distribution of energies of the light-producing electrons both significantly affect the auroral system, and that current connectivity should be studied in three dimensions.

1 Introduction

Laws governing the physics of auroral arc systems are intrinsically three-dimensional—the conservation of mass, momentum, and energy density, in conjunction with Maxwell's equations, outline a system whose across-arc, along-arc, and field aligned directions are coupled. In the last decade or two, interest in three-dimensional (3-D) studies of the auroral ionosphere has slowly picked up (Amm et al., 2008; Fujii et al., 2011, 2012; Marghitu, 2012; M. Zettergren & Snively, 2019; Clayton et al., 2019, 2021; Lynch et al., 2022; Yano & Ebihara, 2021; van Irsel et al., 2024), and we continue this trend by investigating quiet, discrete auroral forms in 3-D. Specifically, this paper looks at how electric current closure and Joule heating are affected by global-scale electric fields, the energy distributions

67 of precipitating electrons, and along-arc structure in field-aligned currents (FAC), to provide
 68 insight into the geophysical domain of auroral arc systems.

69 The conductivity of the ionospheric volume surrounding auroral arcs is highly sensitive
 70 to impact ionization from electron precipitation (Fang et al., 2008, 2010). This ionization
 71 increases with increased energy flux, varies horizontally depending on arc structure,
 72 and varies in altitude depending on the energy distribution of the precipitation. Furthermore,
 73 the overarching, large-scale convection electric field guides the current continuity
 74 solution and directly affects the Joule heating of the system. For these reasons,
 75 to better understand auroral arc system currents, it is crucial that such systems are studied
 76 in 3-D.

77 Auroral-arc-scale science plays an important role in interpreting magnetosphere-
 78 ionosphere-thermosphere (MIT) coupling. The ionospheric end plays a non-passive role
 79 in this coupling (Marghitsu, 2012, & references therein) and is involved in an ongoing sequence
 80 of system science studies (Wolf, 1975; Seyler, 1990; Cowley, 2000; Lotko, 2004;
 81 Fujii et al., 2011, 2012; Marghitsu, 2012; Khazanov et al., 2018; Clayton et al., 2019, 2021;
 82 Yano & Ebihara, 2021; Lynch et al., 2022; Enengl et al., 2023; Wang et al., 2024; van
 83 Irsel et al., 2024). Such MIT studies require F -region ionospheric maps of FAC and electric
 84 potential to be consistent with a 3-D ionospheric conductivity volume created by sunlight
 85 and charged-particle, auroral precipitation. However, what is often looked at is the
 86 two-dimensional (2-D) perspective of auroral arc systems, whether that is north-up or
 87 east-north. In ~~this~~the case of the horizontal ($\perp \mathbf{B}$) perspective, high-latitude electrostatic
 88 coupling assumes the height-integrated relation between quasi-static electric field, FAC,
 89 and conductances given by Kelley (2009, Equation 8.15):

$$j_{\parallel}(x, y) = \Sigma_P \nabla_{\perp} \cdot \mathbf{E} + \mathbf{E} \cdot \nabla_{\perp} \Sigma_P + (\mathbf{b} \times \mathbf{E}) \cdot \nabla_{\perp} \Sigma_H, \quad (1)$$

90 where (x, y) is the plane orthogonal to the local magnetic field, j_{\parallel} is the ionospheric top-
 91 side FAC, $\Sigma_{P,H}$ are the height-integrated Pedersen and Hall conductivities, i.e. conduc-
 92 tances, \mathbf{E} is the ionospheric electric field, and $\mathbf{b} = \mathbf{B}/B$ is the magnetic field direction.
 93 Yano and Ebihara (2021) (among others, Marghitsu, 2012; Fujii et al., 2012) however, have
 94 pointed out that integrating out altitudinal effects can hide significant information re-
 95 garding polar ionospheric systems, especially in terms of current closure. They use sim-
 96 plified 3-D Hall-magnetohydrodynamic simulations, taking into account ion-neutral col-
 97 lisions, to show that 2-D FAC closure assumed by the thin-layer approximation of the
 98 ionosphere is fundamentally different from the 3-D description, if alone for the fact that
 99 current streamlines can pass underneath one another.

100 The electric field solution from Equation 1 can be separated it into a constant, large-
 101 scale electric field, $\bar{\mathbf{E}}$, and a perturbation field, $\delta\mathbf{E}$, which gives two FAC contributions:
 102 $j_{\parallel} = \bar{j}_{\parallel} + \delta j_{\parallel}$ where

$$\bar{j}_{\parallel}(x, y) = \bar{\mathbf{E}} \cdot \nabla_{\perp} \Sigma_P + (\mathbf{b} \times \bar{\mathbf{E}}) \cdot \nabla_{\perp} \Sigma_H, \quad (2)$$

103 and

$$\delta j_{\parallel}(x, y) = \Sigma_P \nabla_{\perp} \cdot \delta\mathbf{E} + \delta\mathbf{E} \cdot \nabla_{\perp} \Sigma_P + (\mathbf{b} \times \delta\mathbf{E}) \cdot \nabla_{\perp} \Sigma_H. \quad (3)$$

104 After calculating and height-integrating the conductivities at a particular point in time,
 105 one can subtract \bar{j}_{\parallel} from a specified F -region map of FAC, j_{\parallel} , with which $\delta\mathbf{E}$ can be de-
 106 termined, i.e. solving current continuity and ionospheric Ohm's law with source term $\delta j_{\parallel} =$
 107 $j_{\parallel} - \bar{j}_{\parallel}$. In this sense, the electrostatic drivers are j_{\parallel} and $\bar{\mathbf{E}}$, and the ionosphere responds
 108 by introducing polarization fields to provide the remaining FAC. In other words, $\delta\mathbf{E}$ is
 109 a result from local polarization charge densities within the ionospheric volume, while $\bar{\mathbf{E}}$
 110 is an electric field external to our auroral-arc-scale system. With this perspective, a
 111 constant global estimate of the background flow, $\bar{\mathbf{v}} = \bar{\mathbf{E}} \times \mathbf{b}/B$, from either SuperDARN
 112 or PFISR, is an additional current driver and thus should be accounted for when inter-
 113 preting FAC observations. Both Equation 1 and topics discussed in this paper deal with
 114 self-consistency, not causal relationships, when finding solutions to auroral current con-
 115 tinuity.

116 Marghitsu (2012) reviews sequentially more complex descriptions of auroral arcs,
 117 the first of which takes on a band of enhanced uniform conductance with negligible al-
 118 titudinal thickness and polarization electric fields that are fully in the across-arc direc-
 119 tion. Having no along-arc gradients whatsoever results in FAC closure which relies only
 120 on Pedersen currents (see Equation 1), while the electrojet current flows underneath, but
 121 plays no part in FAC closure. The second description introduces an along-arc compo-
 122 nent in the electric field which can greatly enhance the auroral electrojet current by means
 123 of the Cowling effect (Cowling, 1932). With a partial Cowling channel (one with some
 124 FAC blockage), Amm et al. (2008) point out that this requires taking into account the
 125 ionospheric thickness when looking at current continuity. This is because, as Yano and
 126 Ebihara (2021) have also pointed out, divergence-free currents cannot flow through one
 127 another. Amm et al. (2011); Fujii et al. (2011, 2012) therefore take on a finite length Cowl-
 128 ing channel model, which includes a thin Pedersen layer on top of a thin Hall layer, al-
 129 lowing for primary and secondary Pedersen and Hall currents to connect. The third de-
 130 scription by Marghitsu (2012) only ignores the along-arc variation in the electric field, but
 131 does take on gradients of conductance along the arc. To understand FAC closure with
 132 this description, Marghitsu (2012) uses 2-D (east-north) modeling given the non-linear
 133 nature of this problem. Marghitsu (2012) concludes, however, that, even though various
 134 one- or two-dimensional descriptions of auroral arcs capture a substantial interpretation,
 135 a complete 3-D description is necessary to fully understand, even sheet-like, auroral arc
 136 systems.

137 This paper builds ~~from~~ work done by Clayton et al. (2021), who study auroral
 138 arc systems and, to do so, developed new methods for driving simulations with 2-D maps
 139 of auroral data to study the surrounding ionosphere in 3-D. Similar to the work presented
 140 in this paper, they use multi-spectral auroral imagery from the Poker Flat [DASC](#)
 141 [Digital All-Sky Camera](#) to both (a) infer the electron precipitation energetics and (b) repli-
 142 cate one-dimensional, in situ measurements of plasma flow, creating continuous 2-D driver
 143 maps. Their plasma flow measurements are provided by the Isinglass sounding rocket
 144 campaign and the replication methods are described by Clayton et al. (2019). In this pa-
 145 per, we use replication methods by van Irsel et al. (2024), which expand upon these ideas,
 146 yet altered slightly in order to use in situ FAC data from orbital spacecraft (Swarm) in-
 147 stead of plasma flow data. With these tools, and given an abundance of observational
 148 datasets from the winter months of 2023, we explore the dependencies of current closure
 149 paths and Joule heating in auroral arc systems ~~to~~ different values of \bar{E} , forms of elec-
 150 tron precipitation spectra, and top-boundary FAC structures.

151 In this paper, we aim to determine geophysical, self-consistent solutions to iono-
 152 spheric current continuity in non-ideal discrete auroral arcs that posses structure in across-
 153 arc, along-arc, and field aligned directions. In doing so, we explore how to properly drive
 154 3-D simulations of auroral arc systems using 2-D electrostatic, continuous top-boundary
 155 conditions from distributed, multi-platform datasets: all-sky, multi-spectral imagery, in
 156 situ FAC data, and radar-based background convection flow data. Additionally, we study
 157 the sensitivity of current continuity solutions to various driver parameters, particularly
 158 background convection flow and precipitation parameters, in order to envelop auroral
 159 arc simulations in a form of qualitative confidence estimates. This provides a better un-
 160 derstanding of the dominant physics behind auroral current closure and Joule heating
 161 for different situations. Ancillary to this, this study provides a catalog of auroral arc sim-
 162 ulations covering six conjunction events with multiple modeling iterations per event, as
 163 well as driver and visualization tools to facilitate future studies of auroral arc systems.

164 In Section 2 we outline the instrumentation used in this work, a brief description
 165 of the ionospheric model used to produce our simulations, along with methods for im-
 166 agery inversion, the replication technique, the implementation of precipitating electron
 167 impact ionization, and our use of flux tubes for 3-D visualization of current closure. Sec-
 168 tion 3 summarizes the 6 conjunction events and Section 4 covers the simulation results

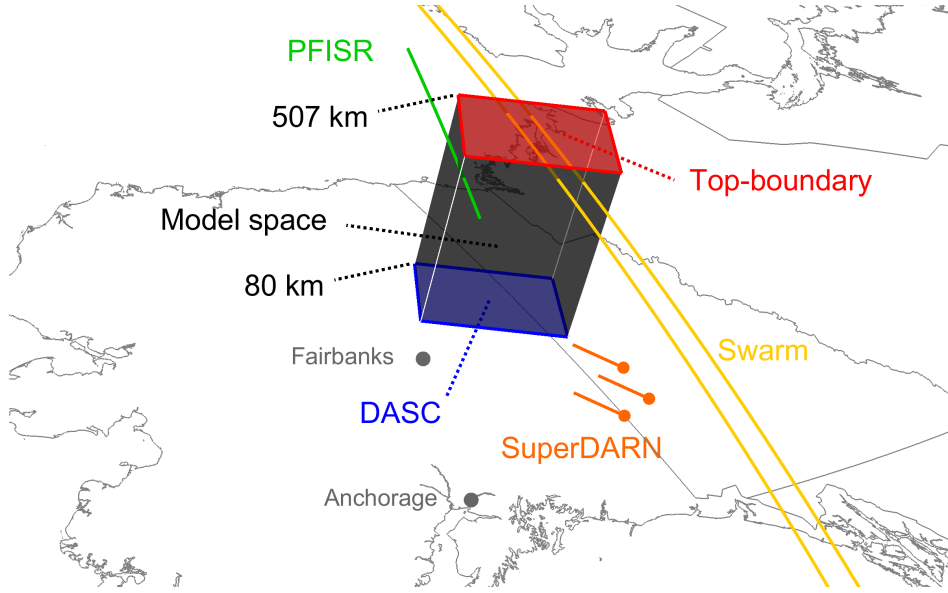


Figure 1. Geographical context of our simulations, using the February 10, 2023 conjunction as an example, showing the model space (black), the Swarm A and C crossings (yellow), the PFISR track (green), the top-boundary for the driver maps (red), the approximate location of the imagery from below (blue), and a symbolic depiction of some flow vectors from the SuperDARN global data map (orange) on top of Alaska.

169 and comparisons thereof. We conclude our findings and discuss possible improvements
 170 and future uses of our work in Section 5. Appendix A covers the derivation of the dif-
 171 ferential hemispherical number flux of accelerated Maxwellian precipitation, and figures
 172 of simulations not included in [the main body of this paper](#) are in the Supporting In-
 173 formation, along with other supporting figures and descriptions.

174 2 Observational Data, Instrumentation, & Methodologies

175 The data products we use are of six conjunction events that are part of the *Swarm-*
 176 *over-Poker-2023* campaign. This campaign facilitated simultaneous observations in Febru-
 177 ary – March, 2023, of a variety of auroral arcs during times when the European Space
 178 Agency’s (ESA) Swarm spacecraft orbited overhead of the Poker Flat Research Range
 179 in Alaska. These observations are of key ionospheric electromagnetic parameters includ-
 180 ing, but not limited to, (1) the ESA Swarm mission’s ion flow data from the Thermal
 181 Ion Imagers (TII, Knudsen et al., 2017) and (2) FAC data derived from its magnetome-
 182 ters (Ritter et al., 2013), (3) convection flow data from AMISR’s Poker Flat Incoherent
 183 Scatter Radar (PFISR, Kelly & Heinselman, 2009; Nicolls & Heinselman, 2007; Heins-
 184 selman & Nicolls, 2008), (4) global convection flow maps from the Super Dual Auroral
 185 Radar Network (SuperDARN, Greenwald et al., 1995), and (5) multi-spectral, all-sky
 186 imagery from the Poker Flat Digital All-Sky Camera (DASC, Conde et al., 2001). [The](#)
 187 [six events are chosen based on them \(a\) occurring during February or March of 2023,](#)
 188 [\(b\) including at least one Swarm crossing with imagery, \(c\) having an unobstructed](#)
 189 [night sky, and \(d\) having one or more arcs that fit the quiet discrete arc descrip-](#)
 190 [tion](#) (Karlsson et al., 2020). Figure 1 shows the geographical context of the February
 191 10, 2023 conjunction event. In this section we cover the details surrounding these data
 192 products and any methodologies applied to them, as well as the model used to create
 193 our auroral arc simulations.

194

2.1 Poker Flat Digital All-Sky Cameras & Imagery Inversion

195

196

197

198

199

200

201

The all-sky, multi-spectral auroral imagery we use comes from the University of Alaska Fairbanks Geophysical Institute’s Poker Flat Digital All-Sky Cameras (DASC, Conde et al., 2001) located at 212.57° east and 65.12° north (geographic). From this imagery we use a Python-based routine and the GLObal airglOW model (GLOW, Solomon, 2017) to produce estimated maps of both total precipitating energy flux, Q_p , and expected energy, $\langle E \rangle$. In this work, the expected energy is either the characteristic energy, E_0 , or acceleration potential, U_a (see Section 2.7).

202

203

204

205

206

207

208

209

210

211

As shown by Rees and Luckey (1974), and later expanded on by several others (Strickland et al., 1989; Janhunen, 2001; Hecht et al., 2006; Grubbs II, Michell, Samara, Hampton, Hecht, et al., 2018; Grubbs II, Michell, Samara, Hampton, & Jahn, 2018), the ratio of green line (558 nm) to red line (630 nm) intensity for emissions driven by electron precipitation mostly depends on $\langle E \rangle$, while the blue line (428 nm) intensity mostly depends on Q_p . Roughly following Grubbs II, Michell, Samara, Hampton, and Jahn (2018), we use GLOW, driven with ionospheric background conditions, to generate a lookup table of emission line intensities for a variety of driving precipitation energy spectra. Each energy spectrum in the table is parameterized by its values of Q_p and $\langle E \rangle$, and GLOW simulates emission line intensities separately for each.

212

213

214

215

216

217

218

After denoising and calibrating the imagery, mapping each color to its rough emission altitude, and removing background brightness, we apply a simple Python routine (<https://github.com/317Lab/asispectralinversion>) (Mule, 2025) that uses the lookup tables to invert each usable pixel of the image to a value of Q_p and $\langle E \rangle$, along with rough error bars associated with the inversion. After inversion, all precipitation maps are Gaussian smoothed in the magnetic northward direction with a window size of 32 km ($\sigma \approx 5.3$ km).

219

2.2 Swarm Spacecraft

220

221

222

223

224

225

226

227

228

229

230

231

The European Space Agency’s Swarm mission consists of three satellites which were launched into nearly polar, low Earth orbits on 22 November, 2013, with the goal of providing highly detailed measurements of variations in the Earth’s magnetic field. We use their version 0401, level 2 FAC data derived down to 1 Hz from the Vector Field Magnetometer (VFM, Ritter et al., 2013) data, along with their version 0302, level 1B Electric Field Instruments data, specifically the 2 Hz TII ion drift measurements (Knudsen et al., 2017; Burchill & Knudsen, 2022). The TII data, like the precipitation maps, are Gaussian smoothed to 32 km, while the FAC data are smoothed to 16 km ($\sigma \approx 2.7$ km) ~~to account for the differential relationship between the \mathbf{E} and $\Sigma_{P,H}$ maps, and j_{\parallel} (see Equation 1) to account for their inherently finer structure.~~ The ion drift measurements have a 100–200 m/s one-sigma accuracy, and are used only in our discussions (Section 5) as a point of comparison with our simulation results.

232

233

234

235

236

237

238

239

We note that the choice of smoothing window, an important and carefully deliberated choice, strongly affects the science scales we can investigate. The specific smoothing window is chosen to match and align the available input data scales; we know that driving the model with inconsistent drivers (i.e., fine-scale fields data and large-scale imagery) leads to spurious signatures. For this study, therefore, we have not fully characterized the dependence on this scale choice. Instead we focus our studies on permutations of input parameters at these scales (i.e. on/off or from instrument A versus instrument B and so on).

240

2.3 Poker Flat Incoherent Scatter Radar

241

242

The Poker Flat Incoherent Scatter Radar (PFISR, Kelly & Heinselman, 2009; Nicolls & Heinselman, 2007; Heinselman & Nicolls, 2008) is an Advanced Modular Incoherent

Scatter Radar facility and has been operational since 2007. PFISR is located at the Poker Flat Research Range (212.53° E, 65.13° N), which is owned by the University of Alaska Fairbanks Geophysical Institute, and the radar is maintained for the US National Science Foundation by SRI International. The antenna boresight points at an azimuth of 15° east-of-north and elevation of 74°. In this paper, we take single-value, uniform averages of plasma drift velocity within the latitude ranges of our simulation regions, and use these averages as large-scale background flow estimates. We use their resolved vector velocity (“vvels”) data based on long pulse experiments with a five minute integration time. These data products are produced by Python scripts found at <https://zenodo.org/records/10892410> (Lamarca & Reimer, 2025). We use these data to provide one plasma drift velocity average per conjunction event.

2.4 Super Dual Auroral Radar Network

The Super Dual Auroral Radar Network (SuperDARN) is comprised of 35+ HF and VHF radars located across the northern and southern hemispheres and is operated by 20 institutions across 10 nations. This paper uses plasma convection flow estimates over Poker Flat, AK—one global estimate per conjunction event—that are interpolated by the pyDARN open-source python library. Greenwald et al. (1995) describe the SuperDARN global-scale network and the pyDARN repository can be found at <https://zenodo.org/records/14796490> (SuperDARN Data Visualization Working Group et al., 2025). SuperDARN convection map data shown in this paper ~~was~~were processed using the FITACF3 algorithm with a spectral width-based Heppner-Maynard Boundary. Both the order and degree of the fit was 6.

2.5 FAC Replication

Our simulations require spatially continuous, topside ionospheric FAC maps. van Irsel et al. (2024) outline how this can be done for electrostatic plasma convection maps. Here we have adjusted their methods for FAC maps instead. The replications can be done using distributed optical data, provided by all-sky, multi-spectral imagery, combined with FAC data tracks, provided by spacecraft or sounding rockets. We first invert the imagery using methods outlined in Section 2.1, from which preliminary estimates of the height-integrated conductivities (conductances) are gathered using Equations 3 and 4 in Robinson et al. (1987). The conductance maps are then queried for two isocontours at user-defined conductance values which are the primary and secondary arc boundaries. With these boundaries, the replication process is as follows:

1. The original FAC data track is translated in the east-north plane by some amount following the primary arc boundary such that the original and replicated data are equal at the primary boundary-track intersections.
2. The replicated data track is scaled in the along-track direction such that the original and replicated data are equal at the secondary boundary-track intersections.
3. This replication is repeated for multiple translations along the arc until the top-boundary is filled with FAC values at a sufficient replication density.
4. The replicated FAC data map is then interpolated onto the simulation grid, providing the top-boundary simulation driver.

For replications whose data lie just outside of the simulation region, the arc boundaries are extrapolated, ensuring sensible matching between FAC and precipitation. For example uses of the (weighted) replication method, see Sections 2.2 and 2.3 in van Irsel et al. (2024). For use of this method with FAC data, the electrostatic enforcement (Section 2.2.3) is omitted and the FAC data is treated as one of the components of the flow data.

291

2.6 GEMINI Simulations

292

293

294

295

296

297

298

299

Simulations for this study use the Geospace Environment Model of Ion-Neutral Interactions (GEMINI, M. D. Zettergren & Semeter, 2012; M. Zettergren & Snively, 2019). GEMINI solves for 3-D electrostatic current continuity and ionospheric Ohm’s law, accounting for changes in state parameters which affect conductivities as it steps forward in time; it calculates the electric field that is consistent with how the top-boundary FAC requirements connect through the ionospheric volume—one whose conductivity is highly sensitive to impact ionization from electron precipitation, which is implemented into GEMINI using methods by Fang et al. (2008, 2010).

300

301

302

303

304

305

306

307

308

309

310

311

312

313

314

GEMINI is a multi-fluid (electrons and six ion species), quasi-electrostatic model with its calculations of particle continuity consisting of chemical production/loss and photo/impact ionization. Calculations of local densities, plasma flows, and temperatures are treated self-consistently and the model includes thermal conduction heat flux, collisional heating, thermoelectric electron heat flux, and inelastic cooling/heating from photoelectrons. This is supplemented with Maxwell’s equations and, at the time of writing, includes no displacement current or magnetic induction. With this, the system is solved through enforcing divergence-free currents, curl-free electric fields, and invoking Ohm’s law. GEMINI can be driven with (aside from maps of precipitation energetics handling impact ionization) a map of FAC *or* electric potential at the top-boundary. When driving GEMINI with a top-boundary map of FAC, a user-specified background electric field, \mathbf{E} , is input separately. GEMINI assumes equipotential magnetic field lines, providing horizontal electric fields that are constant in altitude (Farley Jr., 1959). For a full description of the governing equations solved by GEMINI, see M. D. Zettergren and Snively (2015, Appendix A).

315

2.7 Electron Precipitation Methods

316

2.7.1 Electron Precipitation Energy Spectra

317

318

319

For auroral arc systems, electron precipitation energy spectra, $\phi(E)$, are often assumed to be of a standard unaccelerated Maxwellian form (Fang et al., 2008) whose differential number flux, $\phi_u(E)$, is

$$\phi_u(E) = \frac{Q_p}{2E_0^2} \frac{E}{E_0} \exp\left(-\frac{E}{E_0}\right), \quad (4)$$

320

321

322

where Q_p is the total precipitating energy flux, E_0 is the characteristic energy, and E is the precipitation energy. This has its flux peak at an energy of E_0 , representing the arc energy, however, it also incurs an energy spread of

$$\sqrt{\langle (E - E_0)^2 \rangle} = \sqrt{\frac{\int_0^\infty (E - E_0)^2 \phi_u(E) dE}{\int_0^\infty \phi_u(E) dE}} = \sqrt{3}E_0. \quad (5)$$

323

324

325

326

327

In contrast to this formulation, in auroral situations, there is often an accelerated signature (Evans, 1968; Paschmann et al., 2003), where the energy spread is related to the source region thermal motions, while the peak energy is related to the auroral acceleration region (Evans, 1974). Therefore, we look at an alternative $\phi(E)$; that of an accelerated Maxwellian whose differential number flux, $\phi_a(E)$, is (see [Appendix Appendix A](#))

$$\phi_a(E) = \frac{Q_p}{T_s^2 + (T_s + U_a)^2} \frac{E}{T_s} \exp\left(-\frac{E - U_a}{T_s}\right), \quad E \geq U_a, \quad (6)$$

328

329

330

331

332

where T_s is now the source region characteristic energy, and U_a is the auroral acceleration region potential drop. The energy spread, with $U_a > T_s$, is $\sqrt{\langle (E - U_a)^2 \rangle} = T_s \sqrt{(6 + 2U_a/T_s)/(1 + U_a/T_s)}$. With $U_a/T_s \sim 3$, which is not untypical, this has an energy spread of $\sqrt{3}T_s$. This choice for $\phi(E)$ has decoupled the energy spread and peak energy, which in this case is U_a when $U_a > T_s$, which is the case for all our conjunction events.

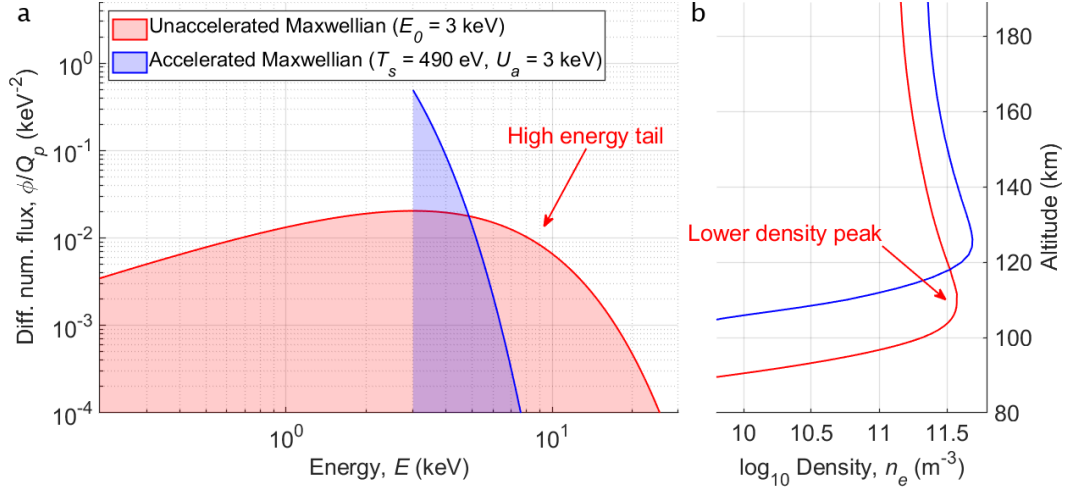


Figure 2. Comparison between unaccelerated and accelerated Maxwellian electron precipitation spectra. (a) Normalized energy spectra of $\phi_u(E)/Q_p$ (red) and $\phi_a(E)/Q_p$ (blue). Note that both spectra peak at 3 keV. (b) Electron density altitude profiles modeled by GLOW (Solomon, 2017) with the same color scheme.

333 Relationships between the acceleration potential and the source region/ionospheric
 334 characteristic energy exists via the FAC this system holds (Knight, 1973; Rönmark, 2002),
 335 but these are not the focus of this paper. Equation 6 is implemented into GEMINI us-
 336 ing methods described by Fang et al. (2010). Both the GLOW model and the methods
 337 described by Fang et al. (2008, 2010) take into account secondary and back-scattering
 338 electrons (Evans, 1974).

339 Figure 2 shows examples of $\phi_u(E)$ and $\phi_a(E)$ (Equation 4 and 6) with $U_a = E_0 =$
 340 3 keV and $T_s = 490$ eV. Both these spectra have the same integrated energy flux, Q_p ,
 341 and both peak at 3 keV, yet the accelerated Maxwellian has a significantly lower energy
 342 spread: 0.8 keV compared to 5.2 keV in the unaccelerated case. Along with this, their
 343 respective electron density altitude profiles are shown, determined using the GLOW trans-
 344 port model (Solomon, 2017). It is evident that the assumption of $\phi_u(E)$ can overesti-
 345 mate the electron density at lower altitudes given the high energy tail of these spectra.
 346 It is noted that a choice of $T_s = U_a = E_0$ has $\phi_a/\phi_u = 2e/5 \approx 1.09$, which therefore does not
 347 change the spectral shape, but merely scales the total energy flux. This suggests that, when using
 348 $\phi_u(E)$, one inadvertently is making the choice of $T_s = U_a$ with $\phi_a(E)$. Additionally, with $U_a = 0$,
 349 i.e. no auroral acceleration, we have $\phi_a/\phi_u = 1$, which covers the relatively low energy
 350 background precipitation surrounding auroral arcs. This fact is what we use to deter-
 351 mine T_s .

352 2.7.2 Determining Source Region Characteristic Energies, T_s

353 The differential number flux for an accelerated Maxwellian population approaches
 354 that of the unaccelerated population as U_a approaches zero. In this limit T_s becomes anal-
 355 ogous to E_0 , thus, in order to find an estimate for T_s , we first invert the imagery (see
 356 Section 2.1) assuming an unaccelerated population, which provides a map of E_0 . Fig-
 357 ure 3, panels a – b, show this map of E_0 and the total energy flux, Q_p , for our Febru-
 358 ary 10, 2023 event.

359 Next, assuming that U_a vanishes outside of discrete auroral arcs, we filter the arc
 360 region out of this map of E_0 by removing pixels corresponding to the top 40th percentile

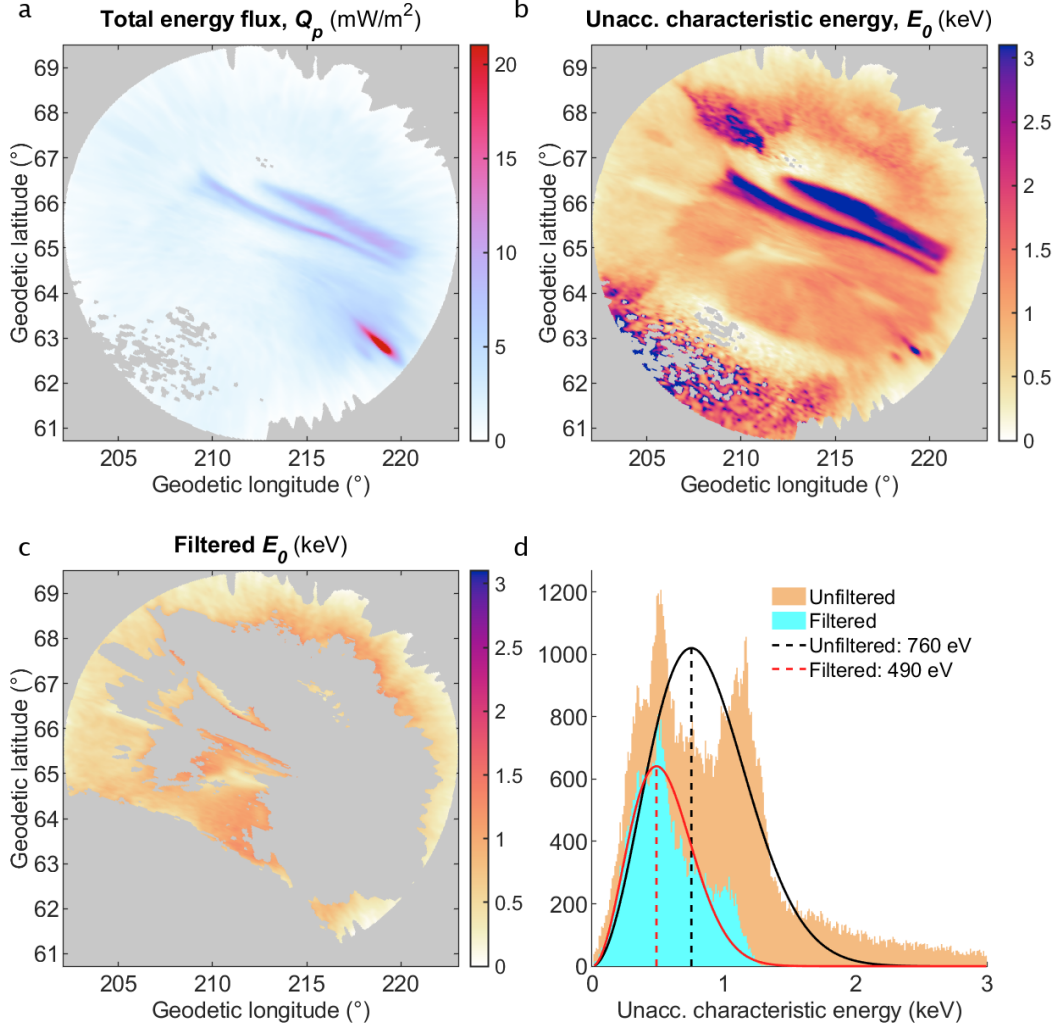


Figure 3. Steps in determining the source region characteristic energy. (a) The total precipitating electron energy flux, Q_p , inverted assuming unaccelerated Maxwellian energy spectra. (b) The characteristic energy, E_0 , inverted assuming unaccelerated Maxwellian energy spectra. (c) E_0 filtered by removing the top 40th percentile of Q_p and the lower 30th percentile of the red line emissions. (d) Histograms of data in panels b (orange) and c (light blue) along with Gaussian magnitude fits (black and red respectively) and their peaks (dashed). Data source: DASC (2025).

of Q_p . We also remove the lower 30th percentile of the red emissions, as the inversion to E_0 performs sub-optimally for lower red intensities. This is shown in Figure 3c. We then look at the histogram of the remaining E_0 values and fit a Gaussian magnitude distribution to it, the peak of which is selected as the source region characteristic energy. In this case, we have $T_s = 490$ eV, as is shown in panel d. This panel also shows the unfiltered distribution which shows two distinct populations, suggesting different physics behind them—presumably that of the accelerated electrons and that of the unaccelerated precipitation.

~~The percentiles used in filtering are chosen by simultaneously minimizing the 95% confidence range and maximizing the adjusted R-squared value of the fits. The different choices for these percentiles raise a rough precision of around $\pm 10 - 20\%$ surrounding the T_s estimations. The choice of top 40th and lower 30th percentiles for the energy flux and red emissions are determined by balancing low 95% confidence ranges and high adjusted R-squared values when fitting the filtered data in Figure 3d. The percentiles investigated for Q_p range from the top 10th – 90th and for the red emissions ranged from the lower 10th – 40th. In this process, we find that the T_s estimates we report have around a $\pm 10 - 20\%$ precision.~~

We assume this value of T_s to be constant over the relevant source region and use it in Equation 6, with which we perform the inversion described in Section 2.1. This inversion now happens over a (Q_p, U_a) parameter space, for a given T_s , instead of (Q_p, E_0) , when creating lookup tables, providing 2-D maps of Q_p and U_a . This is all done for each of the six conjunction events. Reassuringly, we find that inversions of these six events done with either the $\phi_u(E)$ or $\phi_a(E)$ assumptions provide nearly identical maps of Q_p ; however, as we will show, they imply quite different conductivity and current density distributions through the ionosphere.

~~The methodology described in this section, at the time of writing, has not been validated experimentally because the measurement data available in our conjunctions exclude electron spectrometry. We do analyze the different spectral assumptions, and the effect they have on auroral system science, to great lengths in Section 4.2. That said, this methodology invites future studies applying these techniques with multi-spectral imagery data and data used in auroral acceleration region spectrometry (Marghitsu et al., 2006; Imajo et al., 2024)~~

2.8 Current Flux Tube Visualization

In order to visualize current closure in GEMINI output data, we show flux tubes of electric current. GEMINI enforces $\nabla \cdot \mathbf{j} = 0$, where \mathbf{j} is the current density, which makes the usage of flux tubes as a visualization tool sensible. We have developed tools to generate current flux tubes starting at user-defined ellipses contained inside the GEMINI simulation volume. From these ellipses, a number of current vector streamlines are sourced, which, by definition, are tangent to \mathbf{j} throughout the simulation volume. This ensures the current flux through such ellipses is equal to the flux through the orientable surface enclosed by the curve connected by the streamline endpoints. Current fluxes are calculated for tubes that meet flat exit surfaces and are compared against entry fluxes as a check for numerical error. Streamline endpoints that are too far apart, or that meet at a corner of the simulation volume, are locations where the flux tube splits into multiple tubes. In this case, the fluxes of each tube are provided separately. This method of visualization is part of the toolset available [at `https://github.com/317Lab/aurora_geminiOnline`](https://github.com/317Lab/aurora_geminiOnline) (van Irsel, 2025).

Figure 4 shows three example current flux tubes. This $425 \times 288 \times 384$ cell (up, east, north) magnetically aligned volume contains a GEMINI calculated 3-D current density from which the flux tubes are derived. In this paper, simulations are all located in the northern hemisphere and magnetic east, north, and up refer to a locally orthonor-

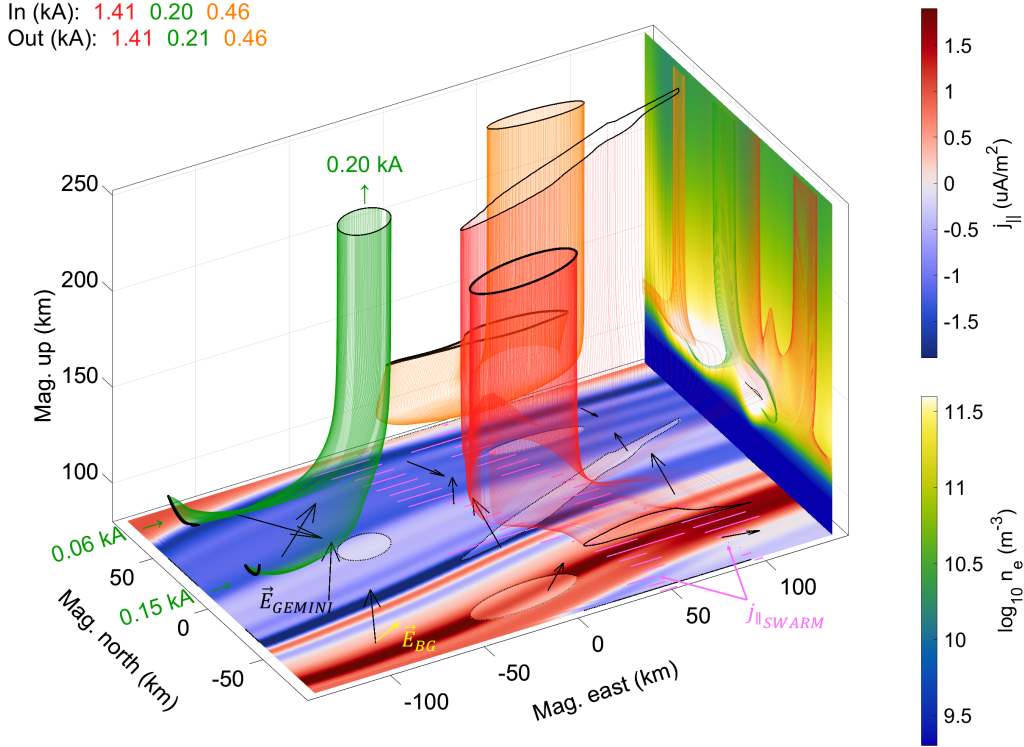


Figure 4. Example of a current flux tube plot using an ~~an example~~ February 10 simulation. The top-boundary FAC driver is plotted at the bottom for visualization purposes. Similarly, a central cut of electron density is plotted at the eastern wall along with flux tube projections. The current flux tubes are color-coded for distinction purposes and start/end at the bold/thin black solid curves. The black dashed lines are their counterparts projected on top of the FAC map. The pink lines indicate FAC data from Swarm A (right track) and C (left track) with parallel being right. The black arrows are a sparse sample of the electric field calculated by GEMINI and the yellow arrow indicates the constant background electric field. Data sources: Swarm (2025), SuperDARN (2025), and van Irsel, J. (2025).

412 mal basis with up being anti-parallel to the local magnetic field, east in the direction of
 413 increasing modified apex longitudes (Laundal & Richmond, 2017), and north complet-
 414 ing the set. The simulation in Figure 4 is driven by a top-boundary map of FAC which
 415 is plotted at the bottom for visualization purposes. The colormap of FAC has red as-
 416 sociated with the downward, parallel-to- \mathbf{B} (in the northern hemisphere) current vector,
 417 also referred to hereinafter as return current (i.e. “red is return”). The blue represents
 418 the upward current (downward-moving electrons in the Northern hemisphere) where, of-
 419 ten, the accelerated auroral electron precipitation is found. On the eastern wall, a cen-
 420 tral cut of electron density is plotted. The density perturbations, which are in most part
 421 the result of the top-boundary precipitation driver maps, govern the 3-D conductivity
 422 volume and thus, in part, the current closure. The black arrows plotted on the FAC map
 423 are a sparse sample of the GEMINI calculated electric field—the second aspect govern-
 424 ing the current closure—and the yellow arrow is the imposed constant, background con-
 425 vection electric field, $\bar{\mathbf{E}}$. The pink lines indicate the FAC current data from, in this ex-
 426 ample, Swarm A and C, that are footpointed down to the top-boundary and plotted at
 427 the bottom as well (these form the basis of the replicated FAC map in red and blue).

428 The current flux tubes are color-coded for easy distinction. In this example, the
 429 red flux tube originates from an ellipse at the top-boundary inside the southernmost down-
 430 ward, return current sheet. It carries 1.4 kA down through the volume, splitting in three,
 431 finding its way out through the top-, south-, and east-boundary. The influx and outflux
 432 regions are outlined by bold and thin closed black curves, and shadows of these curves
 433 are projected to the bottom to visualize which portion of the FAC map they embody.
 434 For select flux tubes, a projection of the entire tube is also plotted on the east-
 435 ern wall. The green flux tube has its user-defined ellipse in the upward current and is
 436 calculated in reverse. It carries around 0.2 kA from two sources on the western wall, com-
 437 bines into a single tube, and connects with the top-boundary. Lastly, the orange flux tube
 438 (also calculated in reverse) is sourced at the northern boundary and also connects to the
 439 upward FAC. Figure 4, and similar figures in the remainder of this paper, display in- and
 440 out-fluxes to two decimal places and illustrate the degree of precision of the flux tube
 441 calculations. Most current flux tubes in this paper are precise up to one decimal place,
 442 with a few exceptions of more complex current flux tubes or ones with higher amper-
 443 age (> 10 kA).

444 3 Conjunction Events

445 This study uses a total of six conjunction events ranging from February 10 to March
 446 19, 2023, from the Swarm-over-Poker-2023 campaign (Poker Flat Research Range, AK).
 447 As a summary of the conjunctions used in this work, Figure 5 shows the top-boundary
 448 selected top-boundary simulation data-drivers for each of the six events: the total en-
 449 ergy flux of the precipitating electrons, Q_p , the acceleration potential, U_a , and the **FAC**
 450 **maps, j_{\parallel} , replicated from the Swarm data.** replicated FAC maps, j_{\parallel} . Driver maps of E_0 or
 451 those of j_{\parallel} using fewer than all available spacecraft are not shown. Also plotted are the
 452 primary and secondary boundaries used in the replication process (see section 2.5) and
 453 the FAC data tracks themselves. In addition, Table 1 displays information regarding which
 454 Swarm spacecraft are part of the conjunction, the activity levels, the PFISR and Super-
 455 DARN background flow estimates, and the rough peak values of the simulation top-boundary
 456 drivers for each event. The distance from Poker Flat to the nearest SuperDARN plasma
 457 flow estimate, \bar{v}_{SD} , is denoted d_{SD} .

458 Not all events have PFISR data tracks available because either they are too far from
 459 their respective, chosen simulation regions, or the data are considered inadequate for our
 460 purposes. Also, not all of the events have a simulation using the unaccelerated assump-
 461 tion for $\phi(E)$. Determining plausible arc boundaries requires meticulous care and deter-
 462 minescontrols where the simulation boundaries are, which is why, for several conjunction
 463 events, the FAC data track(s) lie(s) just east or west of simulation region. In such cases,
 464 the arc boundaries are extrapolated to the data tracks. Following are brief synopses of
 465 each of the six conjunction events after which, in Section 4, we cover their simulation
 466 results.

467 3.1 February 10, 9:51:27 UT

468 Figure 5a – c: This event includes both Swarm A and C cutting through the center
 469 of the simulation around 47 km apart. It has a curved double arc precipitation pat-
 470 tern with each peaking around a total energy flux of $Q_p = 10.0$ mW/m² and accel-
 471 eration potential of $U_a = 5.8$ keV. The precipitation is collocated with the FAC replica-
 472 tion where the precipitating and return current sheets are between $j_{\parallel} = -2.3$ to 2.0 μ A/m².
 473 The PFISR convection flow data are positioned at the western edge of the simulation
 474 space and estimate a strong magnetic westward flow of $\bar{v}_{PF} = (-343, 2)$ m/s. In con-
 475 trast, SuperDARN estimates a nearly stagnant flow of $\bar{v}_{SD} = (-14, 29)$ m/s. The Mag-
 476 netic Local Time (MLT) is 23.1, however, as is shown in Figure 6a, the event occurs 3
 477 – 4 hours duskside of the Harang discontinuity two-cell split.

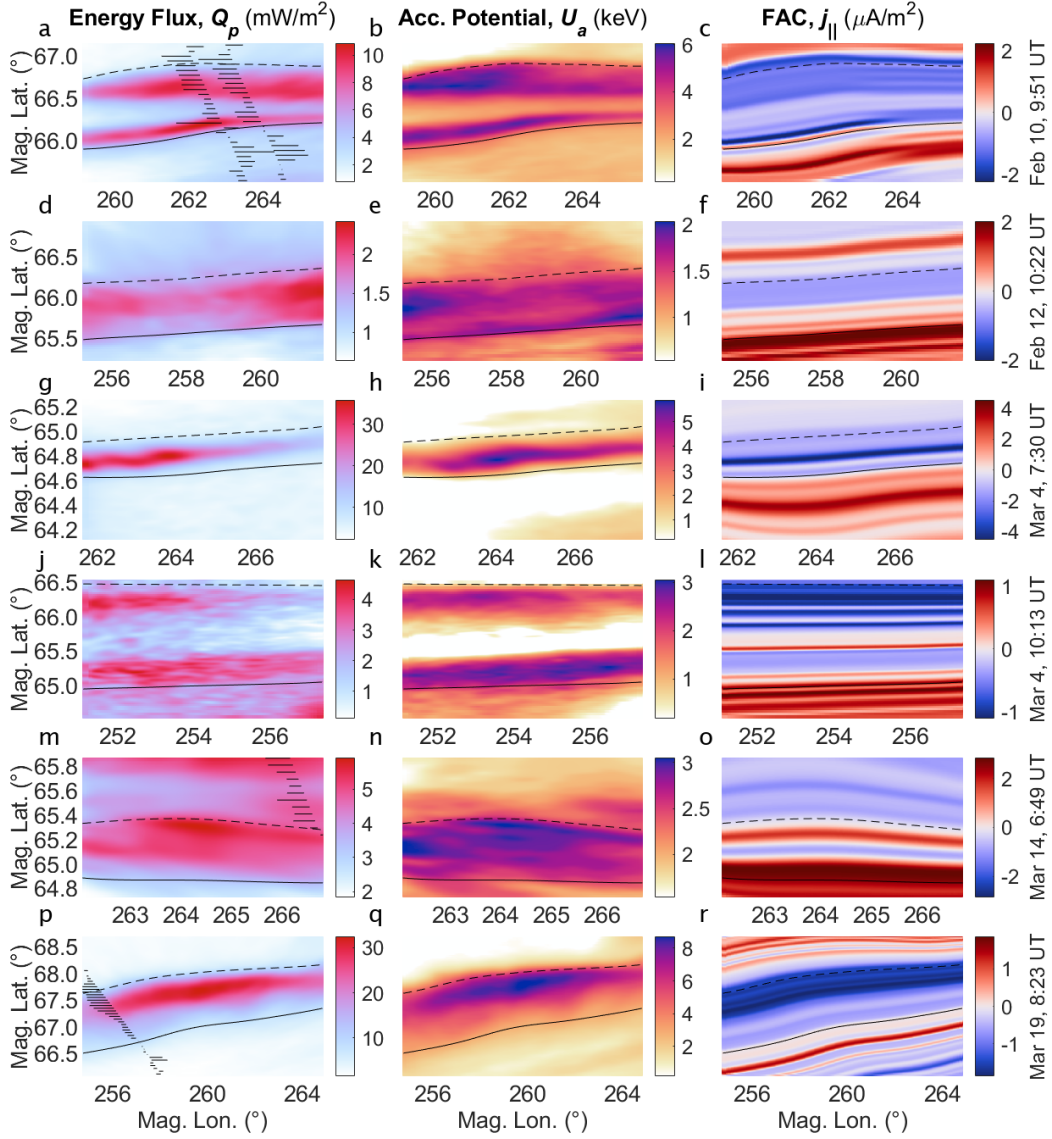


Figure 5. Top-boundary drivers of conjunction events. (a) The total precipitating electron energy flux, Q_p , for the February 10, 9:51 UT event. (b) The acceleration potential, U_a , for the same event. (c) The replicated FAC map, j_{\parallel} , for the same event. (d-r) Same format for remaining events. Note that the respective colorbars change per event. The solid black feather plot indicates the Swarm FAC data tracks with right being parallel. Not all Swarm data tracks are within the simulation volume and are thus not shown. Data sources: Swarm (2025) and DASC (2025).

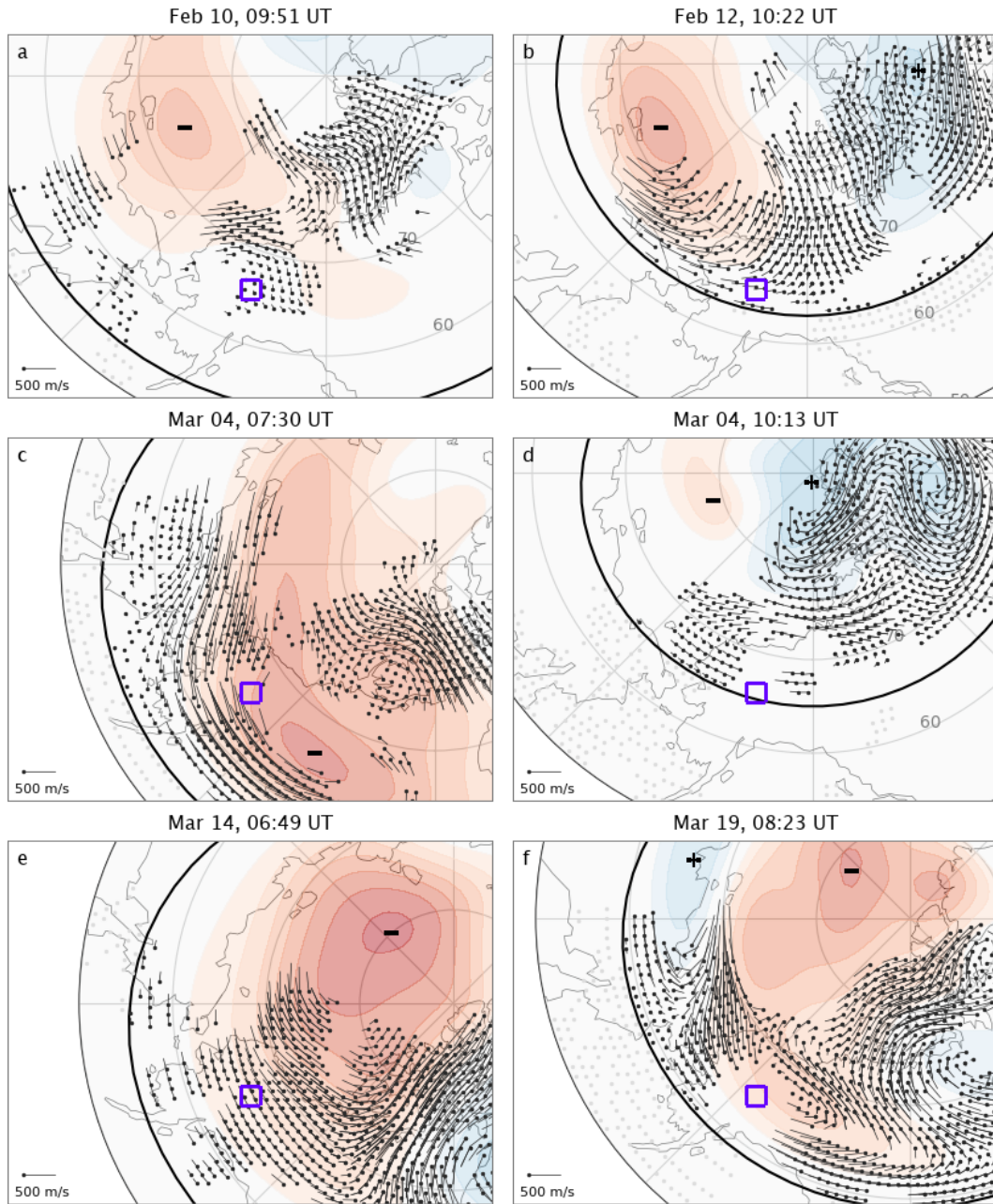


Figure 6. SuperDARN convection maps of conjunction events. Panels a – f represent event IDs 1 – 6 (see Table 1). Purple boxes are approximately centered on Poker Flat, AK and are on the order of the simulation sizes. The bold black line is the Heppner-Maynard Boundary. The colormap shows the electric potential and the “+” and “-” symbols indicate the maximum and minimum potential points. Local magnetic midnight is at the bottom and the dusk side is left. Data source: SuperDARN (2025).

Table 1. Summary of conjunction events with input map values^a.

Event ID	1	2	3	4	5	6
Date	Feb 10	Feb 12	Mar 4	Mar 4	Mar 14	Mar 19
Time (UT) ^b	9:51:27	10:22:11	7:30:12	10:13:49	6:49:07	8:23:30
MLT (Hours)	23.1	23.3	20.7	22.9	20.1	21.4
Region (km) ^c	290 × 182	290 × 189	290 × 126	290 × 225	220 × 126	432 × 291
Swarm S/C	A + C	C	C	B	A + C	B
Ap	15	7	16	16	18	9
F10.7 (a) ^d (s.f.u.)	208 (175)	200 (175)	182 (161)	182 (161)	138 (162)	143 (162)
\bar{v}_{SD} (m/s) ^c	-14, 29	-170, -31	-323, 269	-45, 0	-200, -9	-494, 96
d_{SD} (km) ^c	51	51	184	373	51	375
\bar{v}_{PF} (m/s) ^c	-343, 2	-237, -17	-	-	-418, -44	178, -68
Q_p (mW/m ²) ^f	10.0	2.3	32.3	4.1	5.8	31.3
U_a (keV) ^f	5.8	1.9	5.4	2.9	3.0	8.5
T_s (eV)	490	580	800	860	240	680
E_0 (keV) ^f	4.2	1.4	4.0	2.3	-	-
j_{\parallel} (μ A/m ²) ^f	-2.3, 2.0	-0.7, 1.9	-4.5, 3.8	-1.1, 1.0	-1.2, 2.8	-1.9, 1.4

^aVariables \bar{v}_{SD} , \bar{v}_{PF} , Q_p , U_a , T_s , E_0 , and j_{\parallel} are defined in-text.

^bTimes indicate the spacecraft crossing approximately through the simulation center.

^cRegions and flows are in GEMINI magnetic coordinates/components.

^d[F10.7a is the 81-day F10.7 average centered around the event dates.](#)

^eDistances from Poker Flat to nearest SuperDARN data point.

^fValues for Q_p , U_a , E_0 , and j_{\parallel} are 99% quantiles of maps within a 10 cell border.

478

3.2 February 12, 10:22:11 UT

479

480

481

482

483

484

485

Figure 5d – f: This is a low flux, low energy, and generally inactive event with a Swarm A conjunction roughly 153 km west of the simulation space and with a PFISR data cut through the center. It has a single, blurry but straight arc of around $Q_p = 2.3$ mW/m² and $U_a = 1.9$ keV, with the FAC sheets ranging from $j_{\parallel} = -0.7$ to 1.9 μ A/m². Both PFISR and SuperDARN suggest a large westward flow of $\bar{v}_{PF} = (-237, -17)$ and $\bar{v}_{SD} = (-170, -31)$ m/s respectively. The MLT is 23.3—roughly 1 hour prior to the [Harang discontinuity two-cell split](#).

486

3.3 March 4, 7:30:12 UT

487

488

489

490

491

492

493

494

495

Figure 5g – i: In contrast to the previous event, this one has an intense arc of $Q_p = 32.3$ mW/m² and $U_a = 5.4$ keV with a Swarm C crossing around 141 km eastward of the simulation space and FAC data of $j_{\parallel} = -4.5$ to 3.8 μ A/m². This arc has reasonable along-arc structure; the total energy flux ranges from its peak to around 20 mW/m² going from west to east. Unfortunately, this event does not have usable PFISR data, but SuperDARN shows a very strong northwestern flow of $\bar{v}_{SD} = (-323, 269)$ m/s. This strong, skewed flow is the result of a skewed two-cell convection pattern determined by pyDARN v4.1 (Greenwald et al., 1995) as shown in Figure 6c. The event’s MLT is 20.7, but this convection pattern places it around 5 – 7 hours before the two-cell split.

496

3.4 March 4, 10:13:49 UT

497

498

499

500

501

502

503

504

505

Figure 5j – l: This event, just under three hours later than the previous at an MLT of 22.9, has a straight double arc pattern at $Q_p = 4.1 \text{ mW/m}^2$ and $U_a = 2.9 \text{ keV}$ with Swarm B an average of 94 km westward of the simulation. This event has $T_s = 860 \text{ eV}$, which is 60 eV higher than 2.75 hours earlier (this change is within the $\pm 10 - 20\%$ precision of estimated T_s values), and the currents have now subsided down to $j_{\parallel} = -1.1$ to $1.0 \mu\text{A/m}^2$. Again, this event includes no PFISR data, while SuperDARN now estimates a stagnant flow of $\bar{\mathbf{v}}_{SD} = (-45, 0) \text{ m/s}$. Compared to the previous event, Figure 6d shows a much subdued convection pattern with the Harang region sitstwo-cell split sitting right around local magnetic midnight.

506

3.5 March 14, 6:49:07 UT

507

508

509

510

511

512

513

514

515

516

517

Figure 5m – o: This event is distinct in that it has its precipitation collocated with downward, rather than upward, FAC. There is a down-up-down FAC sheet set ranging from $j_{\parallel} = 2.8$ to -1.2 to $2.0 \mu\text{A/m}^2$ centered around a $Q_p = 5.8 \text{ mW/m}^2$, $U_a = 3.0 \text{ keV}$ precipitation pattern. It is also the second event with both Swarm A and C conjunctions. Swarm A sits around 44 km east of the model space, while the Swarm C crossing is just inside at the northeastern corner, and the southernmost PFISR data point is located around 100 km west of the simulation. The direction of both the PFISR and SuperDARN convection flow estimates are very similar, however, the PFISR flow estimate of $\bar{\mathbf{v}}_{PF} = (-418, -44) \text{ m/s}$ is around twice as strong as the SuperDARN estimate of $\bar{\mathbf{v}}_{SD} = (-200, -9) \text{ m/s}$. This 20.1 MLT event sits at around 2 hours duskside to the Harang discontinuitytwo-cell split.

518

3.6 March 19, 8:23:30 UT

519

520

521

522

523

524

525

526

527

Figure 5p – r: The last event, and the second Swarm B conjunction, is unaligned to magnetic latitudes and has strong precipitation with along-arc structure; the energy flux peaks at around $Q_p = 31.3 \text{ mW/m}^2$ and subsides to around 20 mW/m^2 at the eastern and western boundaries. The acceleration potential is the highest among our events, peaking at around $U_a = 8.5 \text{ keV}$ and the FAC data range from around $j_{\parallel} = -1.9$ to $1.4 \mu\text{A/m}^2$. PFISR cuts through the center and estimates a flow of $\bar{\mathbf{v}}_{PF} = (178, -68)$, where SuperDARN estimates $\bar{\mathbf{v}}_{SD} = (-494, 96) \text{ m/s}$. The MLT is 21.4, however, Figure 6f shows a multi-cell convection pattern which gives a relatively nonstandard context.

528

4 Simulation Results

529

530

531

532

533

534

535

536

537

The six conjunction events are each simulated multiple times, iterating through different parameters, allowing the simulations to be systematically compared. This highlights and isolates the relevant physics involved and allows us to study sensitivities to these parameters. Table 2 provides the list of simulation comparisons covered in this paper (and its Supporting Information), labeled IDs I-XI, where individual simulations are denoted Ia, Ib, IIa, and so on. The comparisons are divided into three categories of feature permutations: (1) background convection flow and its source, (2) the assumption of unaccelerated versus accelerated Maxwellian precipitation spectra, and (3) single versus double spacecraft replications, highlighting along-arc FAC structure.

538

539

540

541

542

543

Each simulation has $425 \times 288 \times 384$ cells in the magnetic up, east, and north directions respectively and are simulated for a duration of 60 seconds with static drivers. The altitudinal extent is 80 – 507 km, with cell heights of 0.3 – 10 km respectively, and the magnetic east/north extents are given in Table 1 and Figure 5. Horizontal cell dimensions settle at 700 – 1400 m in the magnetic east direction, and 238 – 700 m in the magnetic north direction. Unless otherwise stated, all simulations default to SuperDARN

Table 2. Summary of event comparisons^a

Category	ID	Datetime (UT) ^b	BG flow (m/s) ^c		BG source		Acc.	Swarm		
			a	b	a	b		a	b	
Background flow	I	Feb 10, 9:51	(-14, 29)	(-343, 2)	SD	PFISR	Y	-	AC	-
	II	Feb 12, 10:22	(-170, -31)	(-237, -17)	SD	PFISR	Y	-	C	-
	III	Mar 4, 7:30	(-323, 269)	(0, 0)	SD	None	Y	-	C	-
	IV	Mar 14, 6:49	(-200, -9)	(-418, -44)	SD	PFISR	Y	-	AC	-
	V	Mar 19, 8:23	(-494, 96)	(178, -68)	SD	PFISR	Y	-	B	-
Accelerated vs. unaccelerated	VI	Feb 10, 9:51	(-14, 29)	-	SD	-	Y	N	AC	-
	VII	Feb 12, 10:22	(-170, -31)	-	SD	-	Y	N	C	-
	VIII	Mar 4, 7:30	(-323, 269)	-	SD	-	Y	N	C	-
	IX	Mar 4, 10:14	(-45, 0)	-	SD	-	Y	N	B	-
Along-arc structure	X	Feb 10, 9:51	(-14, 29)	-	SD	-	Y	-	AC	A
	XI	Mar 14, 6:49	(-200, -9)	-	SD	-	Y	-	AC	A

^aComparisons are labeled I-XI with individual simulations labeled Ia, Ib, IIa, etc.

^bTimes indicate the spacecraft crossing approximately through the simulation center.

^cPFISR and SuperDARN background flows are in GEMINI magnetic east/north components.

544 background flow estimates, accelerated Maxwellian precipitation, and FAC replication
545 using maximal data tracks. The simulations can be found [at https://reweb.dartmouth.edu/LynchK/Gemini3DOnline](https://reweb.dartmouth.edu/LynchK/Gemini3DOnline) (van Irsel, J., 2025).
546

547 4.1 Background Flow & Electric Field

548 There are two factors which dictate the existence of closure currents: (1) the Pedersen and Hall conductivities, and (2) the strength of the electric field. The conductivities require enhanced ionization at closure altitudes which is largely dictated by electron precipitation—enhanced energy fluxes, Q_p , increase the conductivity overall, while stronger acceleration potentials, U_a , give preference to Hall over Pedersen closure. Adding to this, spatial structure in the precipitation means that these conductivities have 3-D structure, affecting current closure in all directions. The magnitude of the electric field, however, dictates the magnitude of closure currents overall. We argue that strong electric fields can render the need for Hall closure to be negligible. We therefore begin by looking at comparisons of simulations that have different background electric field assumptions.
558

559 Figure 7 shows three view angles of the results for Simulation Ia, referenced in Table 2, where Section 2.8 explains the format of this figure. It uses FAC data from Swarm A and C, the accelerated Maxwellian precipitation assumption, and a background plasma flow estimate from SuperDARN. In this first example, the background flow of $\bar{\mathbf{v}}_{SD} = (-14, 29)$ m/s amounts to a constant background electric field of 1.6 mV/m directed roughly 26 degrees north-of-east (geomagnetic).
564

565 What follows are descriptions of three of our five comparisons (see Table 2) that outline the sensitivity of auroral current closure to the constant background electric field, $\bar{\mathbf{E}}$, around which GEMINI solves current continuity and Ohm’s law for $\mathbf{E} = \bar{\mathbf{E}} + \delta\mathbf{E}$. The remaining comparisons, along with their associated figures and descriptions, can be found in the Supporting Information. [For a more complete 3-D visualization of cur-](#)
569

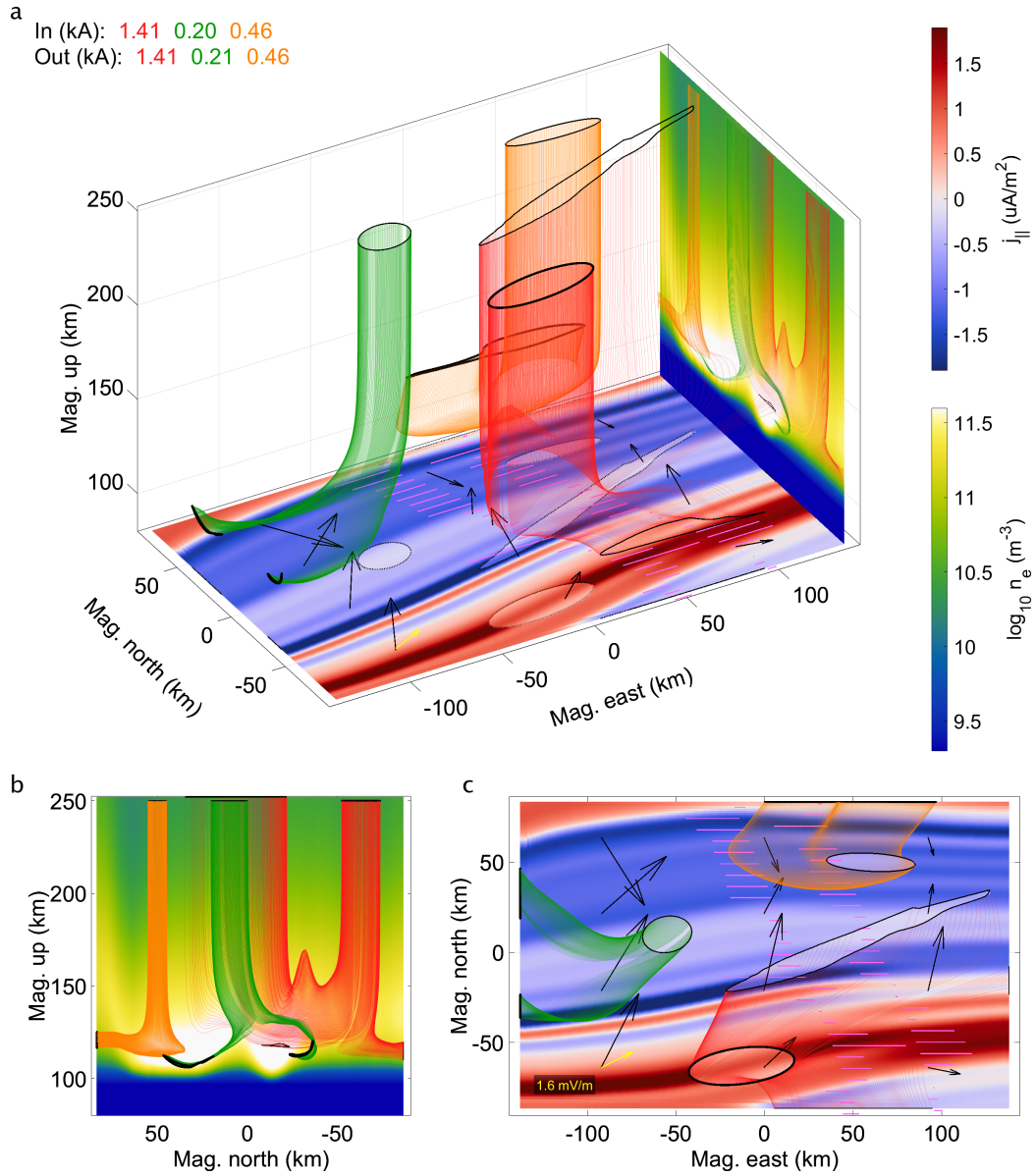


Figure 7. Isometric (a), side (b), and top (c) view of the GEMINI results for Simulation Ia. For plot details, see Section 2.8. Data sources: Swarm (2025), SuperDARN (2025), and van Irsel, J. (2025).

570 rent closure, the Supporting Information also contains isometric views, along with the
 571 side and top views, for all simulations.

572 **4.1.1 Comparison I: Background Flow**

573 In Comparison I, we compare and contrast the use of SuperDARN derived back-
 574 ground flow against using the PFISR observed background flow. Figure 7 illustrates three
 575 current closure paths of Simulation Ia, which assumes the SuperDARN background flow,
 576 and shows the complexity of current closure in a reasonably typical discrete auroral arc
 577 system. The red current flux tube, carrying 1.4 kA, starts at the center of southernmost
 578 return current sheet and rotates to closure currents at an altitude range of 110 – 150 km.
 579 The bulk of the current continues northward, however, 0.2 kA exits through the south-
 580 ern boundary and < 0.1 kA ~~exists~~exits through the eastern boundary. Focusing on the
 581 remaining 1.2 kA, panel c shows that this segment opens up to the northeast, aligning
 582 the tube with the electric field at first, i.e. Pedersen closure. The ~~relatively~~weak strength
 583 of the electric field, however, renders the Pedersen closure ~~ineffective~~ineffective and requires
 584 the tube to traverse through lower altitudes to find sufficient paths for closure. At these
 585 lower altitudes, the Hall currents dominate and thus this portion of the tube rotates per-
 586 pendicular to the electric field. This increases the length it has to travel while crossing
 587 into the upward FAC region and stretches the overall current closure morphology in the
 588 along-arc direction. The portion which exits through the eastern wall, presumably, would
 589 follow this same pattern somewhere outside the simulation volume, but this is specula-
 590 tive. More notably, however, the remaining unclosed portion on the southern part of the
 591 tube traverses southward, but this is for the same reason: the tube rotates in the Hall
 592 layer looking for upward FAC somewhere outside the simulation.

593 The green tube is sourced from the western boundary with two ends, both carry-
 594 ing around 0.1 kA, which combine into a single, 0.2 kA upward segment of the tube clos-
 595 ing in between the two precipitation current sheets. Panel a shows how they cling to the
 596 higher density, i.e. higher conductivity, regions caused by the double-arc precipitation;
 597 they wrap around these density enhancements in the northward direction following the
 598 local electric field.

599 The orange tube is sourced from the northern boundary with 0.5 kA and travels
 600 southward, somewhat aligned to the electric field, before it hits an electric field conver-
 601 gence. Thus, to avoid going against the electric field, the flux tube lowers in altitude,
 602 in search of Hall conductivity, and abruptly turns to the east. This outlines the self-consistency
 603 aspect of the nature of auroral current closure—the flux tube (a) lowers in altitude where
 604 (b) the density is higher, (c) the electric field converges, and (d) the Hall conductivity
 605 increases allowing for an eastward turn, all spatially coincident. Finally, the tube fur-
 606 ther rotates to gain just enough Pedersen current, and hence altitude, to allow for a con-
 607 nection with the upward FAC sheet. This current flux tube, along with the previous two,
 608 highlights a set of 3-D considerations needed when trying to understand current closure
 609 morphology, and thus MIT coupling. This is especially true when Hall currents are re-
 610 quired in this closure, which is the case for Simulation Ia, given its weaker electric field.

611 In contrast, Figure 8 shows three current flux tubes for Simulation Ib (panels c –
 612 d) that capture the same FAC regions, whether at the start or end of each tube. The
 613 only change here is that the simulation now assumes the PFISR derived constant back-
 614 ground flow of $\bar{\mathbf{v}}_{PF} = (-343, 2)$ m/s, which amounts to 17.2 mV/m directed nearly north-
 615 ward compared to the northeasterly 1.6 mV/m from Simulation Ia (panels a – b). This
 616 larger background flow drastically changes the current closure morphology of all three
 617 flux tubes. Given the tenfold increase in the electric field magnitude, on top of a more
 618 direct Pedersen pathway across the arcs, the Pedersen closure has become significantly
 619 more effective. Panels a and c show an increase in closure altitudes of 110 – 150 to 130
 620 – 180 km, which means the Hall layer is virtually untouched by these Simulation Ib clo-

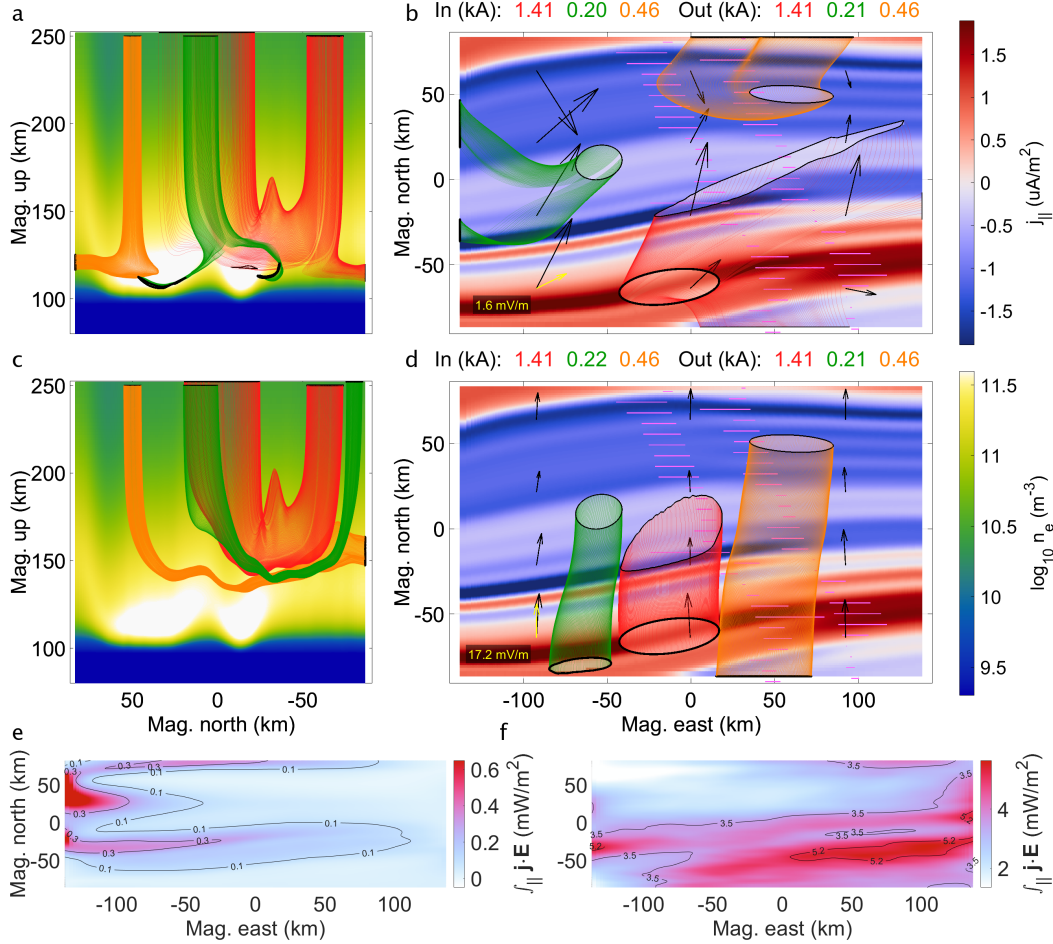


Figure 8. Comparison I (February 10, 9:51 UT): Top and side views of Simulation Ia with SuperDARN derived background flow (a, b) versus Simulation Ib with PFISR derived background flow (c, d) along with height-integrated Joule heating for Simulation Ia (e) and Ib (f). For plot details, see Section 2.8. Data sources: Swarm (2025), SuperDARN (2025), PFISR (2025), and van Irsel, J. (2025).

621 sure patterns. Panel d solidifies this idea, as all three tubes follow the electric fields al-
 622 most directly. This outlines the ability of the background electric field, $\bar{\mathbf{E}}$, to actively drive
 623 auroral arc systems in conjunction with the top-boundary map of j_{\parallel} .

624 To emphasize the sensitivity to the background electric field from the perspective
 625 of energy dissipation, panels e – f of Figure 8 show the height-integrated Joule heating
 626 for Simulations Ia – b respectively. They show the extent to which this auroral arc system
 627 can be an electrostatic load, and how $\bar{\mathbf{E}}$ can change this greatly; aside from having
 628 an order-of-magnitude higher electric field strength, Simulation Ib also closes mostly in
 629 Pedersen currents—parallel to the electric field—both facts favoring higher $\mathbf{j} \cdot \mathbf{E} = \sigma_P |\mathbf{E}|^2$
 630 values throughout. Not only does this increase the Joule heating for Simulation Ib, it
 631 also relocates a bulk portion of it equatorward of the precipitation.

632 The simulations in the next comparison, Comparison III, have a similar disparity
 633 in electric field strengths, yet both have higher FAC requirements, dictating a larger need

634 for closure currents. However, they both also have more precipitation; a factor which par-
 635 tially fulfills this need for additional closure.

636 *4.1.2 Comparison III: Background Flow*

637 The conjunction event for Comparison III, unfortunately, occurs too far from the
 638 PFISR field-of-view and therefore has no PFISR-deduced background flow estimate. Nev-
 639 ertheless, Figure 9 demonstrates the sensitivity to the choice of background flow by look-
 640 ing at Simulation IIIa, where the SuperDARN derived background convection amounts
 641 to 21.0 mV/m directed 40 degrees east of north (first row), and comparing it to Simu-
 642 lation IIIb, which has the background flow set to zero, as there is no estimate for it (sec-
 643 ond row). As explained in Section 1, having zero background electric field amounts to
 644 assuming most of the top-boundary FAC, j_{\parallel} , comes from electric fields caused by local
 645 polarization, $\delta\mathbf{E}$, alone. This comparison shows how much such an assumption affects
 646 current closure. Note that, with $|\bar{\mathbf{E}}| = 0$, for illustration purposes, the electric field la-
 647 bel (black here) indicates the magnitude of the GEMINI calculated electric field vector
 648 shown nearest the label.

649 Comparisons I and III both look at simulations with an order-of-magnitude differ-
 650 ence in their electric field strengths and both cover conjunction events whose accelera-
 651 tion potentials peak at around $U_a = 5$ keV. Comparison III, however, has the precipi-
 652 tation energy flux more than triple, and FAC requirements roughly double, with respect
 653 to Comparison I (see Tables 1 and 2). This creates a higher need for current closure—
 654 a need partially fulfilled by increased conductivity at all altitudes and the strong elec-
 655 tric field strength. Hindering these needs, however, is the less direct path for Pedersen
 656 closure given the roughly 40 degree angle at which the electric field crosses the arc in Sim-
 657 ulation IIIa. The combination of these features allows us to look at how the sensitivity
 658 to electric field strength is affected by a different arrangement of auroral arc parameters.

659 Simulation IIIb, with $\bar{\mathbf{E}} = 0$, depicts a typical perspective of discrete aurora (Marghitu,
 660 2012)—an arc-aligned line of diverging electric field at the downward current sheet, and
 661 a converging one at the upward current sheet, as suggested by Equations 1 – 3. In this
 662 simulation, this is the result of the absence of a background electric field causing cur-
 663 rent continuity and Ohm’s law to be solved with electric fields from local polarization
 664 alone. The red flux tube in Simulation IIIb digs deep into the Hall layer while closing
 665 and is forced to split when bottoming out. This causes 0.4 kA to exit through the south-
 666 ern wall, 0.7 kA through the top-boundary, and < 0.1 kA through the eastern wall. (Note
 667 that this tube loses around 0.2 kA throughout its path which is a result of edge effects
 668 at the eastern wall). In contrast, the order-of-magnitude higher electric field in Simu-
 669 lation IIIa means that its red flux tube carries that 1.4 kA from the return current sheet
 670 across to the precipitation sheet all throughout Pedersen altitudes and, thus, its closure
 671 is directed almost completely in the electric field direction. Contrarily, the green flux tubes
 672 for both simulations close largely with Pedersen currents given that their ends are rel-
 673 atively near one-another. Even though the green Simulation IIIb flux tube finds its clos-
 674 ing currents at lower altitudes, it is still mostly dominated by Pedersen conductivity throug-
 675 out; only the bottom apex of this tube veers to the across- \mathbf{E} direction.

676 Morphologically speaking, the most striking difference between Simulations IIIa and
 677 IIIb lies in their connection to the electrojet current. Figure 9, panels g – h, for Simu-
 678 lations IIIa – b respectively, show a slice of the magnetic eastward component of \mathbf{j} taken
 679 at 50 km west-from-center, along with the intake ends of their respective orange flux tubes
 680 in panels a – d. With its stronger electric field, Simulation IIIa has a much higher elec-
 681 trojet current. [The \$\sim 13\$ mV/m eastward component of the Simulation IIIa electric
 682 field gives rise to a substantial display of the Cowling mechanism enhancing the auroral
 683 electrojet current \(Cowling, 1932; Amm et al., 2011\) as indicated by Figure 9, panels
 684 b and g.](#) This makes this auroral arc system closely resemble a 3-D version of the de-

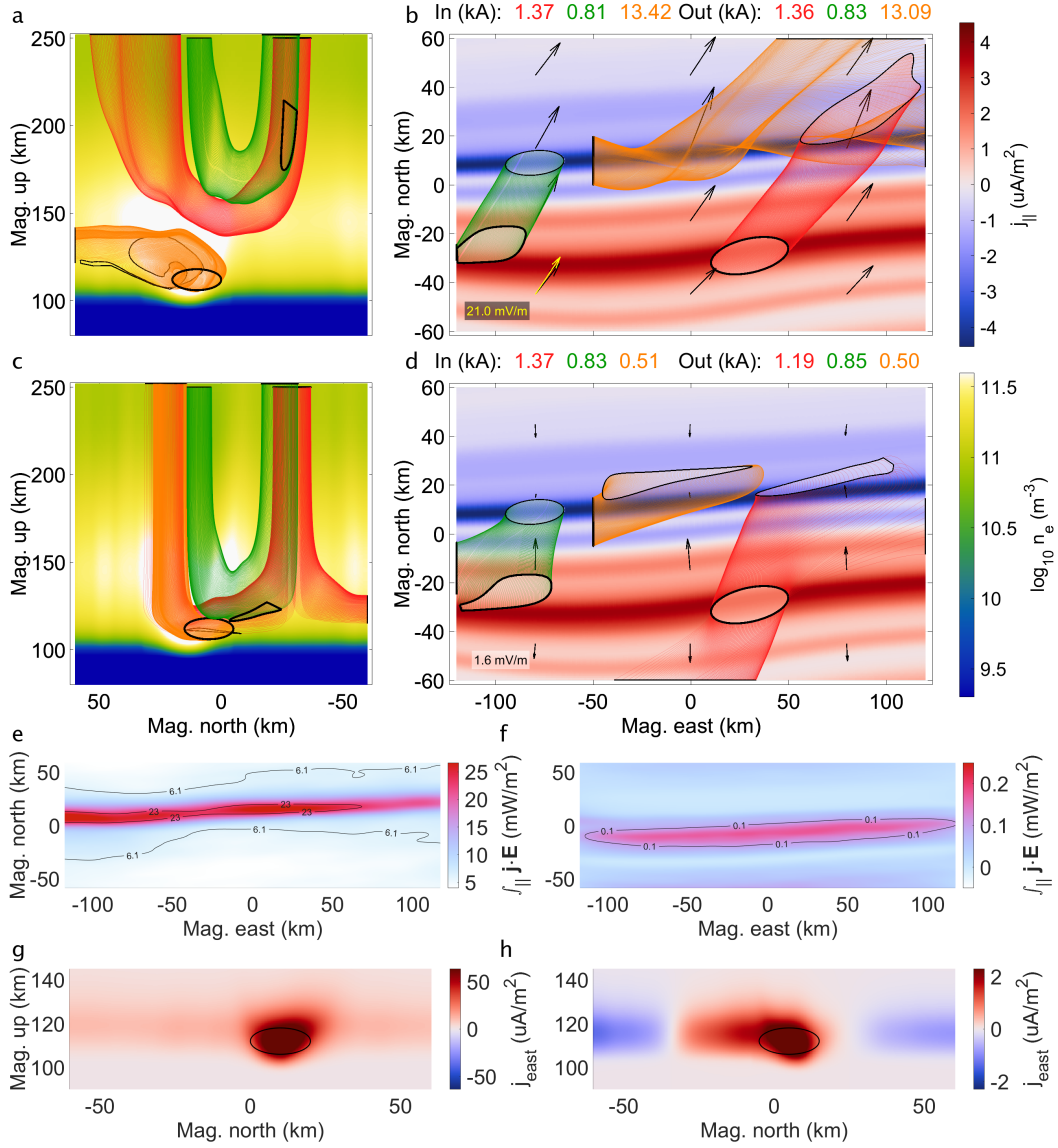


Figure 9. Comparison III (March 4, 7:30 UT): Top and side views of Simulation IIIa with SuperDARN derived background flow (a, b) versus Simulation IIIb with no derived background flow (c, d) along with height-integrated Joule heating for Simulation IIIa (e) and IIIb (f). (g, h) North-up slices of the magnetic eastward current component for Simulations IIIa – b respectively taken at 50 km west from center with the start curves of their respective orange flux tubes (solid black). For plot details, see Section 2.8. Data sources: Swarm (2025), SuperDARN (2025), and van Irsel, J. (2025).

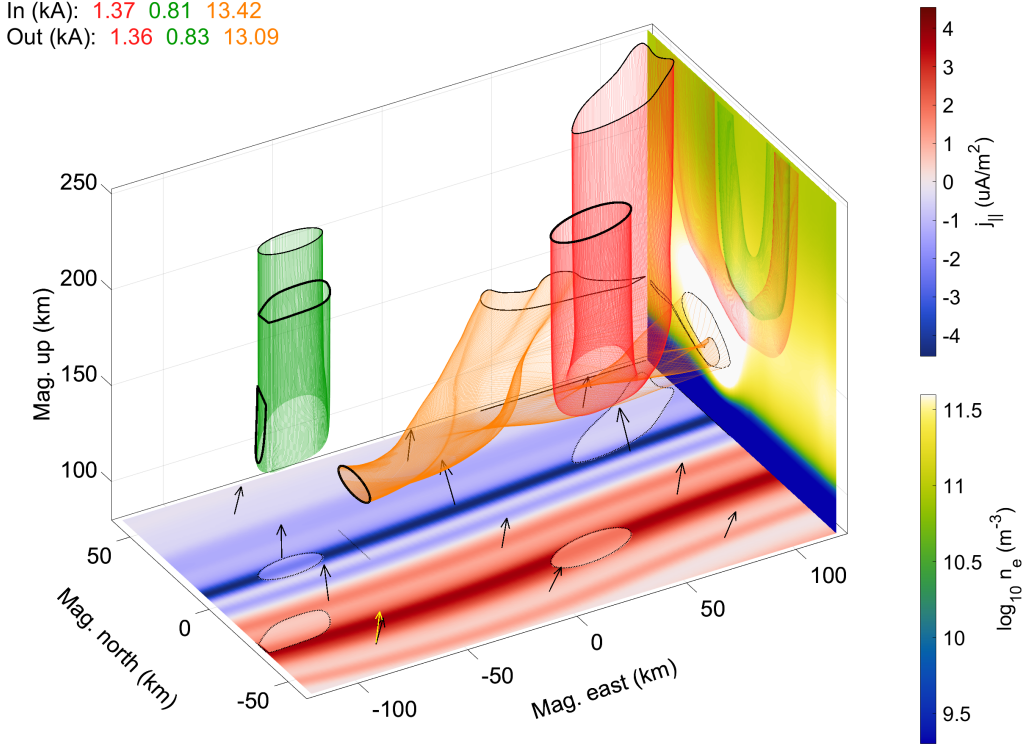


Figure 10. Isometric view of the GEMINI results for Simulation IIIa. For plot details, see Section 2.8. Data sources: Swarm (2025), SuperDARN (2025), and van Irsel, J. (2025).

685 description from Section 4 by Marghitu (2012): A “thick uniform 2-D arc” whose current
 686 closure is separated into a thin Pedersen and Hall layer as shown by Fujii et al. (2012).
 687 Expanding on this description, here we show how current flux tubes can navigate around
 688 each other in a coherent and self-consistent way by venturing into the 3-D perspective.

689 Given the more complex shape of the orange flux tube in Simulation IIIa, Figure
 690 10 shows the isometric view of the simulation results, in addition to the side and top views
 691 in panels a – b from Figure 9. Here we see the almost helical shape of the orange Sim-
 692 ulation IIIa current flux tube, resembling that of Example 3 by Mallinckrodt (1985) but
 693 in 3-D. This tube captures 13.4 kA of the electrojet current, while its Simulation IIIb
 694 counterpart carries around 0.5 kA. Both intake ellipses have the same dimensions and
 695 are centered on their respective peaks of magnetic eastward currents slices. The simu-
 696 lations both have the same relatively strong precipitation arc ($Q_p = 32.3 \text{ mW/m}^2$, $T_s =$
 697 800 keV) around 10 – 20 km north, resulting in a high amount of impact ionization at
 698 relatively lower altitudes. This provides plenty of Hall conductivity and, thus, has both
 699 simulations susceptible to strong electrojet currents. These currents, however, are still
 700 proportional to the electric field strength which is why the order-of-magnitude increase
 701 in electric field results in a similarly increased electrojet current.

702 The enhanced electrojet current in Simulation IIIa does not partake in parallel cur-
 703 rent closure, whereas the Simulation IIIb electrojet current *is* required in the coupling
 704 of magnetospheric currents. As mentioned before, the lower electric field strength over-
 705 all renders all closure currents less effective, hence the FAC has to rely on enhanced conductivity—
 706 Pedersen and then Hall—to connect. Naturally, Simulation IIIa is a more energetic con-

707 figuration in terms of Joule heating; the integrated Joule heating peaks are at around
 708 26.6 mW/m^2 and 0.17 mW/m^2 for Simulations IIIa – b respectively, as shown in pan-
 709 els e – f of Figure 9. This is consistent with the order-of-magnitude difference in elec-
 710 tric field strengths, given the $|\mathbf{E}|^2$ relationship. Given that Hall currents are dissipation-
 711 less (Kaeppler et al., 2012), Simulation IIIb is thus able to rely on the electrojet currents
 712 for closure instead. In Simulation IIIa, the electrojet largely is assumed to follow the global-
 713 scale convection pattern D-shaped Hall currents instead, and ~~is much less involved~~ has neg-
 714 ligible involvement in auroral FAC closure. This electrojet current does, however, con-
 715 nect with Pedersen currents as shown in Figures 9a – b and 10.

716 As with Comparison I (as well as II and IV in the Supporting Information), here,
 717 yet again, we see that a sufficiently large background electric field has FAC close with
 718 Pedersen currents, and thus in the direction of the electric field. Even with the less-direct
 719 Pedersen pathway for closure and the higher FAC requirements, the strong electric field
 720 and relatively large precipitation energy flux provides sufficient conductivity at higher
 721 altitudes and renders Pedersen closure to be the dominant method in MIT coupling for
 722 Simulation IIIa. Furthermore, the Simulation IIIb solution features a distinct $\nabla \cdot \mathbf{E}$ sig-
 723 nature. In Simulation IIIa, however, this signature is masked by the its large background
 724 electric field (compared to no background field in Simulation IIIb). This emphasizes the
 725 dominance of the $\nabla \Sigma_{P,H}$ terms in balancing the FAC map for auroral systems with large
 726 electric fields. Next, we move onto Comparison V whose simulations both have strong
 727 electric fields, yet in severely different orientations.

728 **4.1.3 Comparison V: Background Flow**

729 Simulation Va assumes a background electric field of 25.2 mV/m directed 11 de-
 730 grees east of magnetic north as estimated by SuperDARN. In the almost complete op-
 731 posite direction to this, Simulation Vb has PFISR estimate 9.5 mV/m directed 21 de-
 732 grees west of south. This results in drastic differences in both current closure morphol-
 733 ogy and Joule heating, as depicted by Figure 11. Both the red and green flux tubes com-
 734 pletely flip directions in their current closure. The green flux tube, in its attempt to con-
 735 nect to the broad, primary precipitation current sheet, changes from sourcing its roughly
 736 5.3 kA from the southwest corner in Simulation Va, to doing so from the northern end
 737 in Simulation Vb. The red flux tube, closing the southern primary downward current
 738 sheet, simply flips direction by following the electric field, and, interestingly, in both sim-
 739 ulations it ends up skipping over an adjacent, lesser downward current sheet when clos-
 740 ing its 0.8 kA .

741 As shown in panels g – h of Figure 11, the orange flux tube, like in Comparison III,
 742 captures the electrojet current for both Simulations Va – b. (Here, the user-defined el-
 743 lipse sits at 0 km east and the tube is calculated in both directions.) As expected, this
 744 flux tube also flips its orientation, with the current flowing from west-to-east in Simu-
 745 lation Va, and east-to-west in Simulation Vb. However, like in Comparison III (Figure
 746 9) but to a lesser extent, the weaker electric field strength in Simulation Vb requires the
 747 need of this electrojet current to help close some of the FAC, 0.3 kA in this case. The
 748 62% weaker field also has reduced this Hall current flux tube by about 52%.

749 As in Comparisons I and III, the height-integrated Joule heating shown in panels
 750 e – f of Figure 11 varies roughly in proportion to the electric field strength squared. One
 751 notable difference, however, lies in the tapering off of this Joule heating in simulation
 752 Vb. This indicates that the western boundary of this simulation relies more on Hall clo-
 753 sure; an idea supported by the electrojet usage in FAC closure depicted by the orange
 754 flux tube in panels c – d. Regardless of the reasoning behind this, Comparison V has shown
 755 that a mere directional change in the background electric field can create different dis-
 756 sipation characteristics of an auroral system. Moreover, Comparison V highlights how
 757 the direction of the background electric field completely changes the connectivity of a

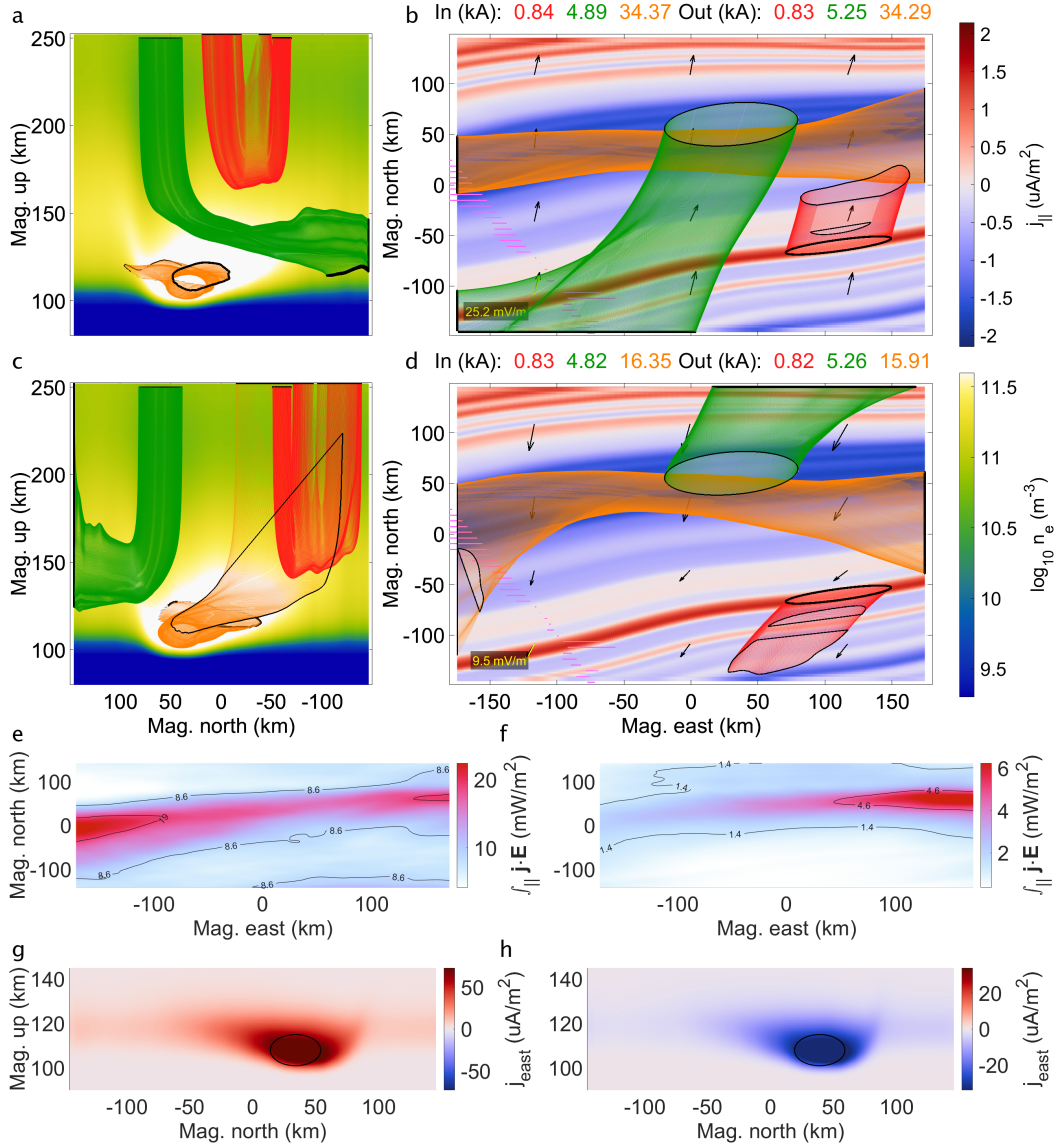


Figure 11. Comparison V (March 19, 8:23 UT): Top and side views of Simulation Va with SuperDARN derived background flow (a, b) versus Simulation Vb with PFISR derived background flow (c, d) along with height-integrated Joule heating for Simulation Va (e) and Vb (f). (g, h) Central north-up slices of the magnetic eastward current component for Simulations Va – b respectively with the start curves of their respective orange flux tubes (solid black). For plot details, see Section 2.8. Data sources: Swarm (2025), SuperDARN (2025), PFISR (2025), and van Irsel, J. (2025).

758 given map of FAC. It is tempting to assume that a precipitation current sheet connects
 759 with its closest adjoining return current sheet, but as we have shown here, knowledge
 760 of the global-scale convection has considerable influence when it comes to FAC connec-
 761 tivity.

762 **4.1.4 Summary: Background Flow**

763 Auroral arc systems are very sensitive to the electric field in matters of current clo-
 764 sure. Given that there are many self-consistent solutions for \mathbf{E} in Equation 1 that can
 765 be considered geophysical, we have shown here that it is crucial to get a good estimate
 766 of the global background flow in order to properly interpret behavior at auroral arc scales.
 767 In terms of simulation confidence, we can have more trust in simulations whose sources
 768 for background electric field estimates agree, such as Comparisons II and IV. However,
 769 when attempting to best understand the auroral arc system pertaining to a particular
 770 conjunction event, more certainty is needed for systems like those shown in Comparisons
 771 I, III, or V. Future conjunction campaigns will therefore benefit greatly from dedicated,
 772 multi-platform observations of large-scale convection flow—observations of comparable
 773 importance to in situ FAC measurements.

774 Previous studies have looked at how the strength and direction of the ionospheric
 775 electric field alters auroral current closure by systematically dividing the field-aligned,
 776 Pedersen, and Hall currents into primary and secondary components (Amm et al.,
 777 2011; Fujii et al., 2011, 2012). In this work, we look at an undivided, 3-D current con-
 778 nectivity in which primary and secondary polarization currents blend into a set of
 779 individual current flux tubes. The reader is encouraged to compare and contrast these
 780 two perspectives and recognize the sub-current mechanisms within the flux tubes them-
 781 selves.

782 **4.2 Electron Precipitation Spectra**

783 As discussed in Section 2.7, the choice of precipitating electron energy spectra can
 784 affect the impact ionization rate at different altitudes; an unaccelerated Maxwellian pro-
 785 file, Equation 4, often carries an erroneous high-energy tail which overestimates the E -
 786 region density enhancement from electron precipitation. Moreover, choosing to use un-
 787 accelerated Maxwellian spectra in inverting multi-spectral imagery results in a de facto
 788 source region characteristic energy equal to the accelerating potential drop, i.e. $T_s =$
 789 $U_a = E_0$. This is not unlike how a choice of $\bar{\mathbf{E}} = 0$ carries hidden assumptions about
 790 j_{\parallel} (see Equations 2 – 3). With an accelerated Maxwellian profile, Equation 6, we es-
 791 timate T_s prior to multi-spectral image inversion which allows for much “colder” source
 792 populations and, we argue, more geophysical precipitating electron modeling.

793 Below are two comparisons which look at how decoupling the source region char-
 794 acteristic energy from the auroral acceleration potential changes auroral current closure.
 795 See Table 2 for details on these comparisons and Table 1 for the (peak) values for Q_p ,
 796 U_a , T_s , and E_0 .

797 **4.2.1 Comparison VI: Precipitation Spectra**

798 Returning back to the February 10 conjunction event from Comparison I, Figure
 799 12 depicts Comparison VI which looks at the differences between Simulation VIa (also
 800 named Ia) with the accelerated precipitation spectra assumption given by $\phi_a(E)$ (first
 801 row), and Simulation VIb which assumes $\phi_u(E)$ instead (second row). The first feature
 802 to point out is the central, north-up electron density slices shown in panels a and c: sim-
 803 ulation VIa has both precipitation arc induced density enhancements tucked above 100
 804 km in altitude, while the use of $\phi_u(E)$ in Simulation VIb has these same two arcs increas-
 805 ing their electron density enhancements to the bottom of the simulation volume. This

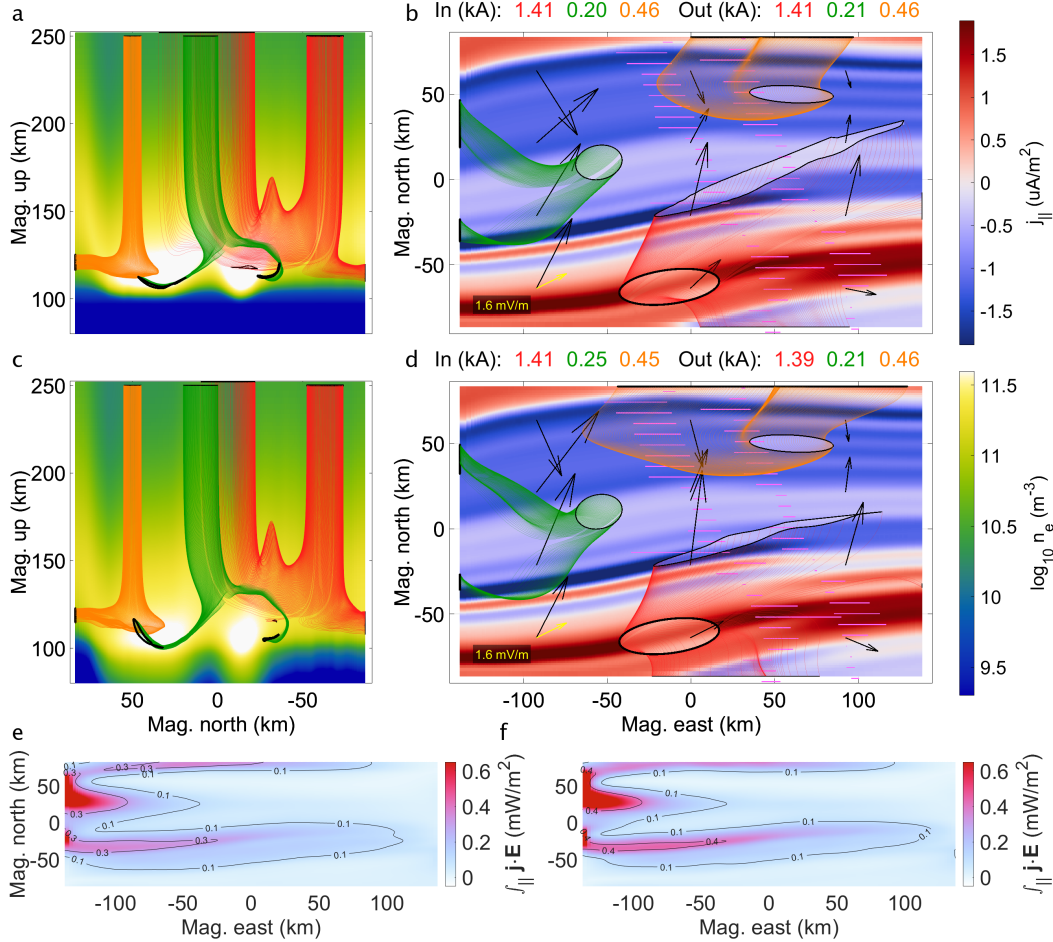


Figure 12. Comparison VI (February 10, 9:51 UT): Top and side views of Simulation VIa with accelerated Maxwellian electron precipitation (a, b) versus Simulation VIb with unaccelerated Maxwellian electron precipitation (c, d) along with height-integrated Joule heating for Simulation VIa (e) and VIb (f). For plot details, see Section 2.8. Data sources: Swarm (2025), SuperDARN (2025), and van Irsel, J. (2025).

806 limits the closure paths of current flux tubes in Simulation VIa, compared to Simula-
 807 tion VIb.

808 Panels a and c show that all three current flux tubes are squished to higher alti-
 809 tudes in Simulation VIa, compared to Simulation VIb, forcing them to have a preference
 810 of Pedersen, over Hall, current closure. Panels b and d show how this affects the curva-
 811 ture of the flux tubes from a topside view. The red flux tube in Simulation VIa extends
 812 significantly further north given its preferred direction of that of the electric field, whereas
 813 the Simulation VIb red flux tube stays more parallel to the arc, traveling perpendicu-
 814 lar to the electric field. Note that, despite the morphology being more along-arc, this flux
 815 tube does not extend much further east compared to the one in Simulation VIa, as it is
 816 able to capture higher upward FAC densities in this direction. Subsequently, its end re-
 817 gion has a smaller overall area needed to capture 1.5 kA of upward FAC. Similar to the
 818 red flux tubes, the Simulation VIb orange current flux tube travels more often in the di-
 819 rection perpendicular to \mathbf{E} compared to its Simulation VIa tube, again because the flux
 820 tube is able to traverse lower altitudes.

821 Panels e – f show that, in this instance, the height-integrated Joule heating increases
 822 by around 30% with the unaccelerated, over the accelerated, Maxwellian precipitation
 823 assumption. This can be counterintuitive when considering the Pedersen closure pref-
 824 erence of Simulation VIa. Looking at panels b and d of Figure 12, however, tells us that
 825 the electric fields (black arrows) surrounding the arcs are higher in strength with the un-
 826 accelerated assumption which, evidently, is consistent with an increase in Joule heating.
 827 Ultimately, along with having the same FAC and background electric field drivers, both
 828 simulations have near identical maps of total precipitating electron energy, even though
 829 their imagery inversions assume two different spectral shapes. This implies that the al-
 830 titudinal distribution of impact ionization alters the energy accounting, and thus the elec-
 831 tric load characteristic of this auroral arc system.

832 Both Simulations VIa – b assume the relatively weak, SuperDARN derived $|\bar{\mathbf{E}}| =$
 833 1.6 mV/m, which makes them more susceptible to changes in the Hall closure layer as
 834 we have shown in Section 4.1. Adding to this susceptibility, the precipitation arcs have
 835 relatively high values of $U_a = 5.8$ and $E_0 = 4.2$ keV respectively. This deposits the
 836 impact ionization to lower altitudes, rendering the Hall layer more important still. This,
 837 along with the altered Joule heating, puts emphasis on the energy distribution shape of
 838 precipitating electrons in such auroral systems. Up next, we look at Comparison VIII
 839 whose simulations have both much stronger background electric fields and significantly
 840 higher total precipitation energy flux, which, along this line of reasoning, implies both
 841 Simulations VIIIa – b are less reliant on Hall closure in MIT coupling.

842 **4.2.2 Comparison VIII: Precipitation Spectra**

843 The precipitation arcs in Simulation VIIIa (also named IIIa) assume an accelera-
 844 tion potential peaking at around $U_a = 5.4$, and the characteristic energy for the arcs
 845 in Simulation VIIIb reach around $E_0 = 4.0$ keV—similar to the values from Compar-
 846 ison VI. However, with respect to Comparison VI, the simulations in Comparison VIII
 847 have more than three times the energy flux, $Q_p = 32.3$ mW/m², background electric
 848 fields that are more than 13 times stronger, $|\mathbf{E}| = 21.0$ mV/m, and FAC sheets whose
 849 magnitudes around double, $|j_{\parallel}| = 3.8 - 4.5$ μ A/m². Additionally, at $T_s = 800$ eV, the
 850 source region characteristic energy for simulation VIIIa also nearly doubles that of Sim-
 851 ulations VIa. Figure 13 shows how unaccelerated Maxwellian precipitation at these more
 852 energetic parameters compares to accelerated Maxwellian precipitation.

853 By proxy of the electrojet currents shown in panels g – h, the unaccelerated Maxwellian
 854 precipitation deposits ionization to both lower altitudes—around 6 km lower compared
 855 to Simulation VIIIa—and to a larger altitudinal range given the nearly four times higher
 856 energy spread of the unaccelerated energy spectra. We focus on these electrojet currents
 857 by looking at both orange flux tubes, which capture similar values of 13.1 and 14.8 kA
 858 for Simulations VIIIa – b respectively. As before, the density volume resulting from the
 859 accelerated Maxwellian assumption is restricted to above around 100 km, forcing the re-
 860 spective orange tube to take on more Pedersen current. This means the electrojet in Sim-
 861 ulation VIIIa veers to the northeast, directed toward the electric field (see panel b). The
 862 orange flux tube in Simulation VIIIb, being overall at lower altitudes, travels more east-
 863 erly, staying relatively orthogonal to the electric field.

864 As shown in panels a – b, the red flux tube in Simulation VIIIa takes advantage
 865 of the energy deposition at higher altitudes and the large electric field strength, and finds
 866 closure through Pedersen alone. In Simulation VIIIb, however, only around 0.7 of the
 867 1.4 kA is able to connect with the FAC, while the remainder ~~exists~~exits through the east-
 868 ern boundary. Interestingly, the existence of the electrojet current in Simulation VIIIb
 869 appears to push the red flux tube away from the highest densities, subsequently squeez-
 870 ing it to lower altitudes. The green flux tube, having to travel a shorter horizontal dis-
 871 tance compared to the other tubes, remains at altitudes where the $\phi_u(E)$ versus $\phi_a(E)$

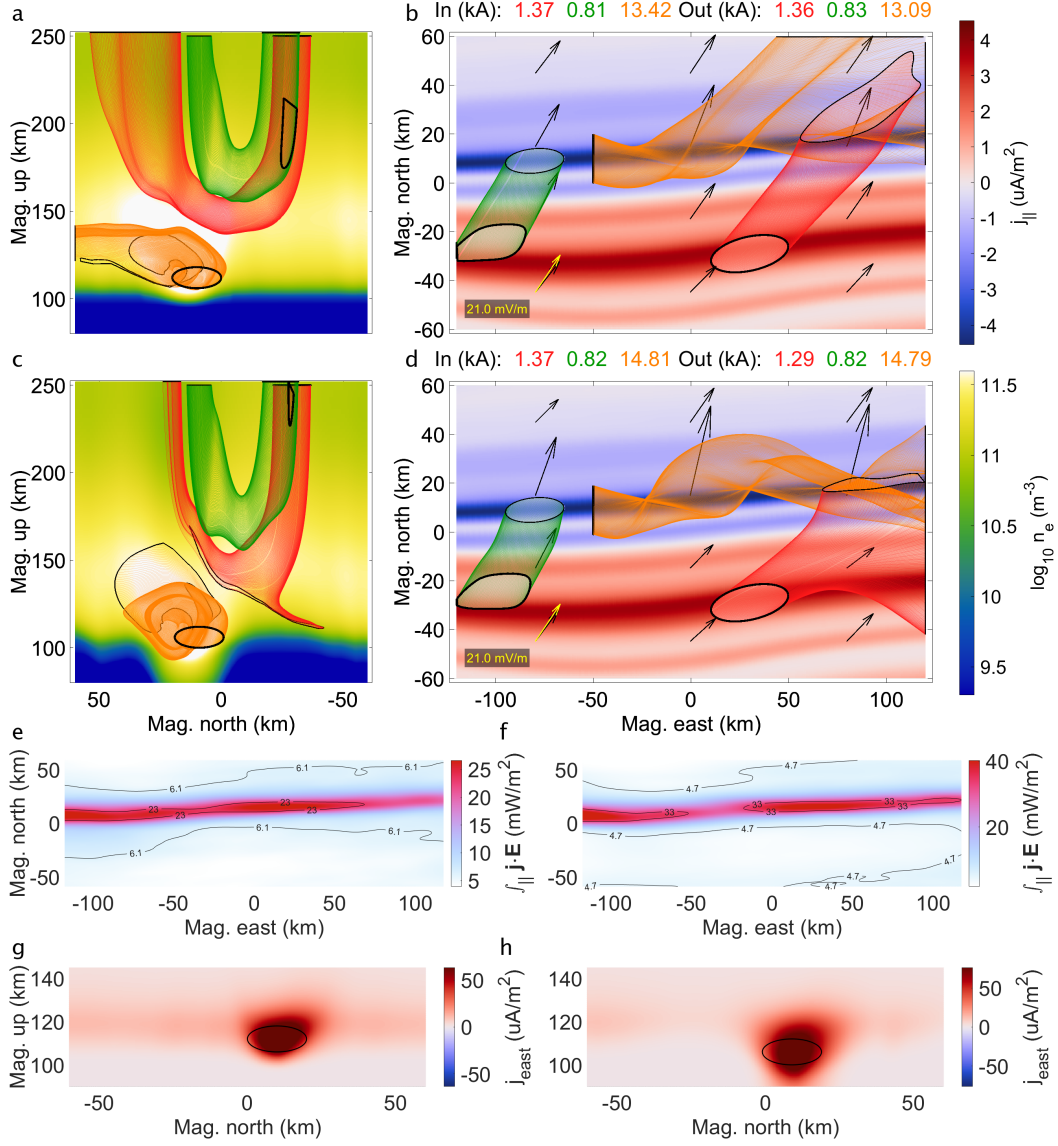


Figure 13. Comparison VIII (March 4, 7:30 UT): Top and side views of Simulation VIIIa with accelerated Maxwellian electron precipitation (a, b) versus Simulation VIIIb with unaccelerated Maxwellian electron precipitation (c, d) along with height-integrated Joule heating for Simulation VIIIa (e) and VIIIb (f). (g, h) North-up slices of the magnetic eastward current component for Simulations VIIIa – b respectively taken at 50 km west from center with the start curves of their respective orange flux tubes (solid black). For plot details, see Section 2.8. Data sources: Swarm (2025), SuperDARN (2025), and van Irsel, J. (2025).

872 assumption matters much less, and so it barely changes its morphology and amperage
873 across the two simulations.

874 Panels e – f of Figure 13 show a band of enhanced Joule heating just equatorward
875 of the precipitating arc in both simulations, yet Simulation VIIIa has this band peak at
876 around 26.6 mW/m^2 , while Simulation VIIIb peaks closer to 40.0 mW/m^2 —around a
877 50% increase. Between the two simulations, the Pedersen current density remains fairly
878 similar; it is the significantly varying Hall current density that creates the different mor-
879 phologies (see Figure 14, panels a – d). This points to the electric field strength; in Sim-
880 ulation VIIIa there is a band of enhanced across-arc electric field collocated with the Joule
881 heating and peaks at around 20 mV/m , while the same is true for Simulation VIIIb ex-
882 cept that it peaks around 40 mV/m (see panels e – f).

883 The bands of precipitation enhanced Hall conductance for Simulations VIIIa – b
884 peak at around 60 and 80 S respectively, as shown in panels g – h. Now, since their spa-
885 tial morphology comes from the same imagery, it implies that this increase in peak value
886 also increases $\nabla_{\perp} \Sigma_H$, enhancing its associated FAC contributions as per Equation 1. Pan-
887 els i – j show that these contributions, in this case, are in the opposing direction with
888 respect to the total FAC driver—the third term in Equation 1 creates an upward cur-
889 rent sheet where the driver map expects a downward sheet, and vice-versa. Given that
890 the second term, $\mathbf{E} \cdot \nabla_{\perp} \Sigma_P$, can only help balance this by increasing $|\mathbf{E}|$, it would do
891 so equally to that third term, $(\mathbf{E} \times \mathbf{b}) \cdot \nabla_{\perp} \Sigma_H$. This leaves the local polarization to help
892 balance the FAC, as is evident in panels k – l of Figure 14. As before, all the input maps
893 have nearly the same spatial morphology for both simulations, ~~hence,~~. This is why, to
894 increase $\nabla_{\perp} \cdot \mathbf{E}$, the simulation assuming an unaccelerated spectrum has a higher peak
895 electric field, resulting in enhanced Joule heating despite the dissipationless Hall current
896 enhancement.

897 ~~In all, even though Simulations VIIIa – b both have high total energy flux and strong elec-~~
898 ~~tric field strengths, the large FAC requirements and the higher electron energy distribution peaks~~
899 ~~mean that these systems do touch on the Hall layer in their current closure.~~ Simulations VIIIa –
900 ~~b both have intense total energy flux and strong electric field strengths. Both of these~~
901 ~~qualities aid in high-altitude FAC closure. Both simulations, however, also have large~~
902 ~~FAC requirements and higher electron energy distribution peaks—qualities which, all~~
903 ~~else held equal, suggest the need for lower-altitude-reaching FAC flux tubes. Given the~~
904 ~~self-consistent nature of our auroral arc simulations, we can only hypothesize that a~~
905 ~~more moderate FAC top-boundary driver would result in less need for Hall closure,~~
906 ~~but it could also be true that this would result in a Cowling mechanism with reduced~~
907 ~~electric field strength. In contrast, Comparisons VII and IX (see Supporting Informa-~~
908 ~~tion) both pertain to auroral arc systems whose FAC requirements, precipitation energy~~
909 ~~fluxes, and energy distribution peaks are relatively low. These combinations of param-~~
910 ~~eters, even in the case of a weaker electric field in Comparison IX, results in simulations~~
911 ~~whose assumption of electron energy distributions matter less in both current closure and~~
912 ~~Joule heating as a result of FAC source term balancing.~~

913 4.2.3 Summary: Precipitation Spectra

914 We have shown that, if a particular auroral arc system requires Hall currents for
915 FAC closure, choosing unaccelerated Maxwellian energy spectra for precipitating elec-
916 trons is too restrictive when attempting to best represent the resulting impact ioniza-
917 tion. Decoupling the energy spread from the most probable energy allows the modeling
918 of auroral arcs whose electrons are accelerated from much colder source regions compared
919 to their acceleration potential. Even for relatively “hot” accelerated precipitation, such
920 as that from Comparisons VIII and IX ($T_s = 800 - 860 \text{ eV}$), the alternate, unacceler-
921 ated choice of $U_a = T_s = E_0$ still grossly overestimates the depth reached by the elec-
922 tron density enhancements. Holding FAC demands constant, this matters most when the

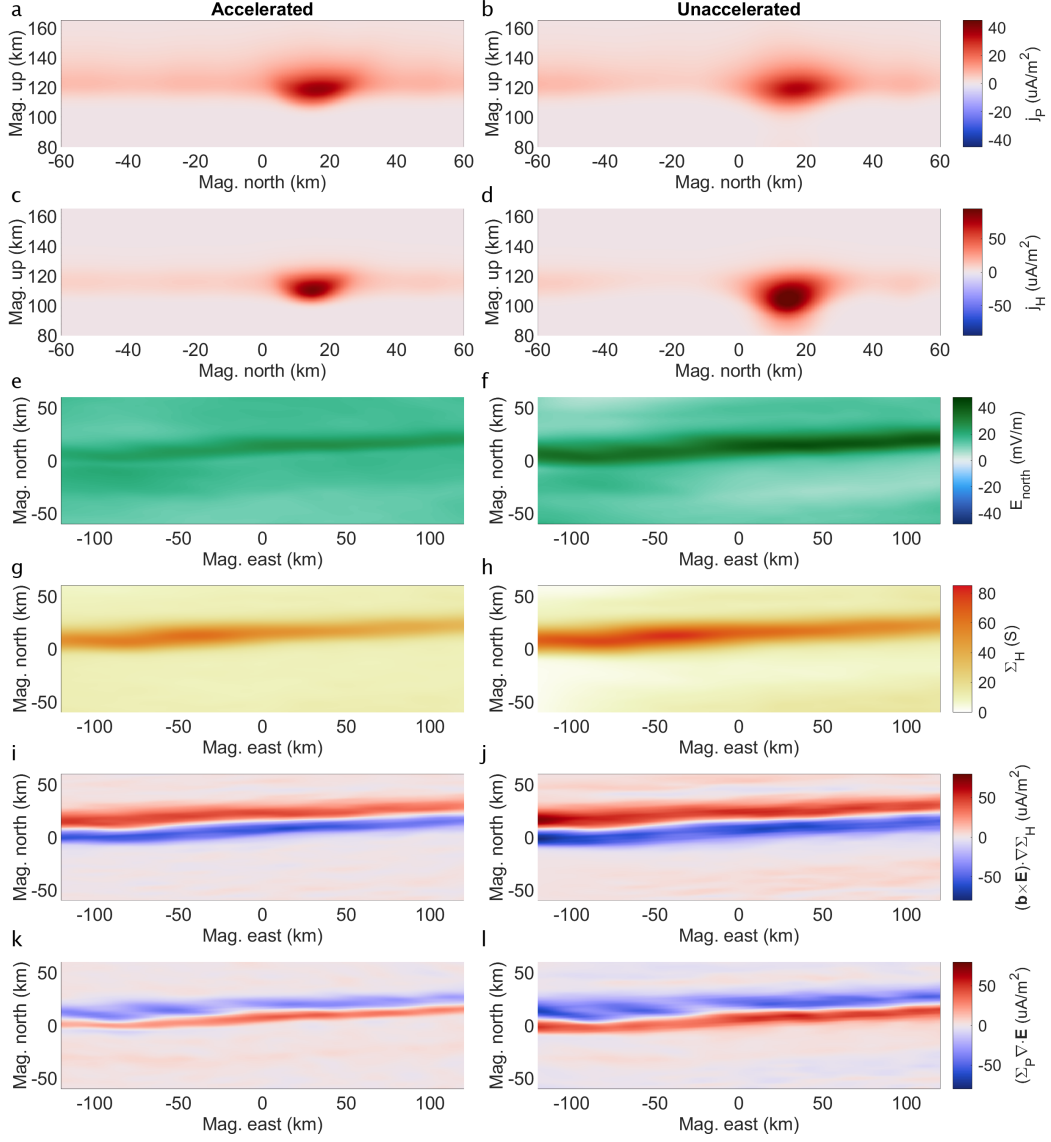


Figure 14. Factors that play a role in enhancing Joule heating for Simulation VIIIb over VI-IIa. (a, b) Central up-north cuts of Pedersen current for Simulation VIIIa – b. (c, d) Same for Hall current. (e, f) East-north plots of electric field’s magnetic north component from Simulation VIIIa – b. (g, h) Same for Hall conductance. (i, j) East-north plots of the third term in Equation 1 for Simulation VIIIa – b. (k, l) Same for the first term in Equation 1. Data sources: van Irsel, J. (2025).

923 average electric field strength is sufficiently weak, and/or the precipitation is low-reaching,
 924 i.e. any factor that puts emphasis on the Hall conductivity layer. Furthermore, unac-
 925 celerated Maxwellian electron distributions can overestimate the Hall currents as a whole,
 926 as well as the height-integrated Joule heating.

927 We have shown that specific assumptions of electron precipitation spectra can change
 928 the interpretation of auroral arc systems. Aptly, recent increases in the availability of
 929 multi-spectral, overrather than white-light, all-sky imagery allows the community to move
 930 away from the assumption of unaccelerated Maxwellian precipitation spectra, and to-
 931 ward energy distributions which decouple the energy spread from the peak energy, al-
 932 lowing for more flexibility in modeling electron precipitation.

933 4.3 Along-Arc FAC Structure

934 Of our six conjunction events, two have a double-spacecraft arc crossing. This gives
 935 us an opportunity to look at two sensitivities: (1) how does along-arc structure in FAC
 936 affect current closure, and (2) how much confidence can be had in the replication tech-
 937 nique we use. Our double replications have a weighting scale length of 50 km (roughly
 938 the distance between the orbits of Swarm A and C) when transitioning from replications
 939 of either track. This is described in more detail by van Irsel et al. (2024, Section 2.3).
 940 When performing a weighted replication with plasma flow data, this can result in arbi-
 941 trary along-arc gradients which affect the first term in Equation 1. In our case, though
 942 the along-arc gradient in j_{\parallel} resulting from this weighting scale length is arbitrary, such
 943 gradients have less physical implication on the system as a whole these gradients do not directly
 944 enter into Equation 1. I.e. the source of error these gradients introduce are the same
 945 as those introduced by the replication technique. Following are comparisons between
 946 double versus single replications of our two double-spacecraft conjunction events.

947 4.3.1 Comparison X: Along-Arc FAC Structure

948 Comparison X looks at our February 10 conjunction event with Simulation Xa us-
 949 ing a weighted replication of both Swarm A (east) and C (west), and Simulation Xb which
 950 uses a replication of Swarm A data only. Their orbits cut roughly through the center of
 951 the simulation volume at about 47 km apart, which allows us to look at current closure
 952 on either side of the tracks. Looking at Figure 15, panels b and d, reveals an up-down
 953 FAC sheet pair that exists in Simulation Xa, but not in Xb. From the western bound-
 954 ary, centered around 40 km south-from-center, a roughly -2 to 1 $\mu\text{A}/\text{m}^2$ FAC pair fol-
 955 lows the arc boundary up until just past the Swarm C FAC data track, from which this
 956 signature is replicated. Furthermore, the southernmost downward FAC sheet narrows
 957 and intensifies, when transitioning from the Swarm A to C tracks, from about 25 km wide
 958 and 1 – 1.5 $\mu\text{A}/\text{m}^2$ in magnitude, to around 10 km and 2 $\mu\text{A}/\text{m}^2$. Simulation Xb has
 959 this FAC sheet remain unchanged along the arc.

960 With these differences in replicated FAC maps in mind, Simulation Xa (Figure 15a
 961 – b), though being the same as Simulation Ia, here shows a different set of current flux
 962 tubes. They are calculated (in reverse) from ellipses placed at the southernmost upward,
 963 precipitating current sheet located east of, west of, and in between the two FAC data
 964 tracks. This helps illustrate the affect on current closure resulting from the difference
 965 between the two data tracks. Figure 15c – d (Simulation Xb) shows flux tubes that are
 966 calculated from the same three ellipses.

967 The orange flux tube (0.5 kA) lies almost entirely east of the Swarm A track, hence
 968 it remains mostly unchanged, both in morphology and quantity. The green flux tube,
 969 however, is encroaching on the aforementioned Swarm C replicated FAC pair and thus
 970 captures around 0.1 kA more in Simulation Xb. The electric field across the arc has the
 971 flux tubes directed southwest to northeast, such that the green flux tube has its influx

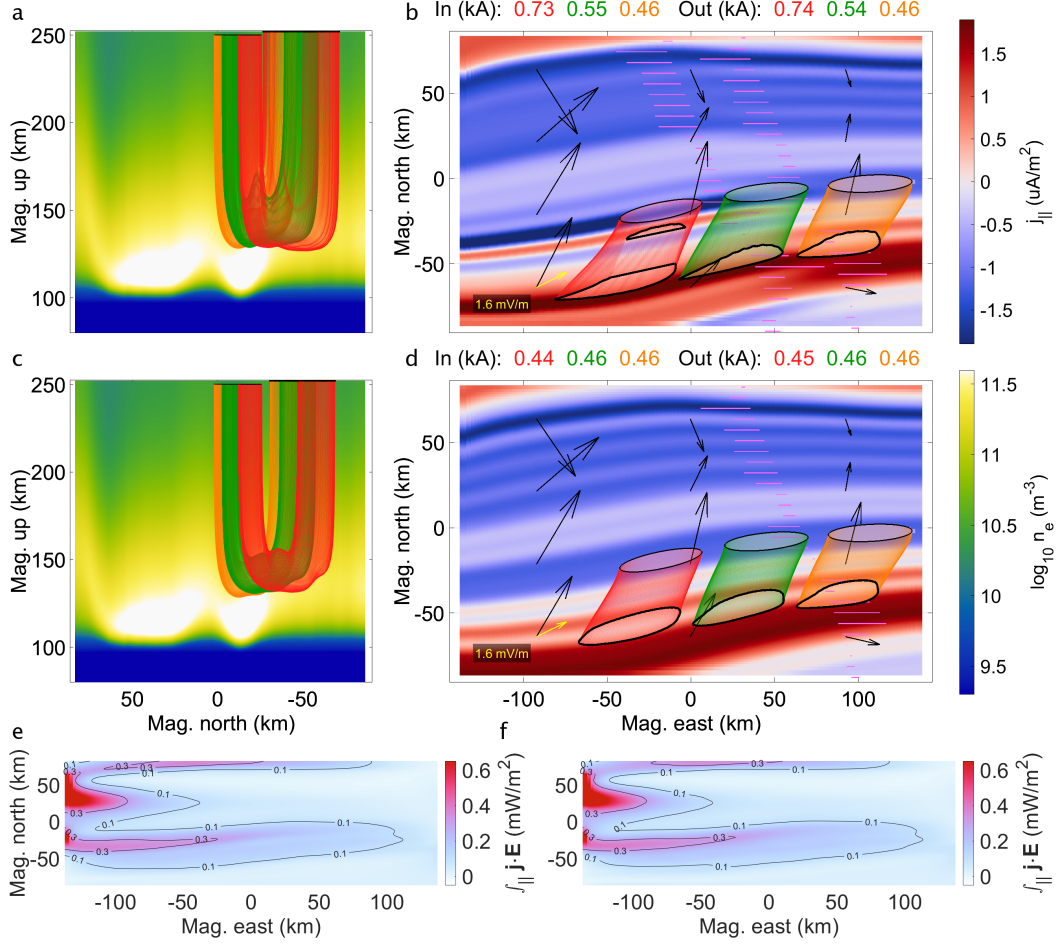


Figure 15. Comparison X (February 10, 9:51 UT): Top and side views of Simulation Xa with a FAC replication using both Swarm A (east) and C (west) (a, b) versus Simulation Xb with a FAC replication using only Swarm A (c, d) along with height-integrated Joule heating for Simulation Xa (e) and Xb (f). For plot details, see Section 2.8. Data sources: Swarm (2025), SuperDARN (2025), and van Irsel, J. (2025).

972 end entirely on the western side of Swarm C. Here, the Simulation Xa downward cur-
 973 rent sheet is stronger, but less than half the width compared to its Simulation Xb coun-
 974 terpart. The steeper FAC across-arc gradient in Simulation Xa pinches the downward
 975 green flux tube end into a teardrop shape ([at roughly 25 km east and 50 km south](#)),
 976 while its higher FAC density aids in capturing that additional 0.1 kA.

977 The red flux tube lies completely on the western side of Swarm C and captures the
 978 upward part of the FAC sheet pair introduced by Swarm C. At 0.7 kA, this gives it an
 979 additional 0.3 kA over the red flux tube in Simulation Xb. The adjacent downward cur-
 980 rent sheet helps close 0.1 kA of this added current, while the remainder is closed with
 981 a similar teardrop shaped flux tube end.

982 Comparison X outlines how a double versus a single FAC data track replication can
 983 introduce, albeit relatively minor, FAC signatures in the along-arc direction. We have
 984 to assume such signatures can appear and disappear over distances on the order of 50
 985 km in every FAC replication. The major FAC structure, however, is conserved, suggest-
 986 ing the replication methodology holds.

987 **4.3.2 Comparison XI: Along-Arc FAC Structure**

988 Due to limitations of the all-sky imagery of the March 14 conjunction event, the
 989 simulation region for Comparison XI is almost completely west of both Swarm tracks.
 990 This prevents us from sourcing current flux tubes on either side of the data tracks, how-
 991 ever we can still use Comparison XI to provide insight into what confidence can be had
 992 in the replication technique, and deliberate about the extent to which auroral arc FAC
 993 varies in the along-arc direction.

994 Panels a – b in Figure 16 show results from Simulation XIa, which is driven by a
 995 FAC map replicated from both Swarm A and C data. However, given the locations of
 996 the data tracks, most of this replication uses data from Swarm C, as it is the closest to
 997 the simulation region. With Simulation XIb (panels c – d) using only Swarm A in its
 998 FAC replication, this is essentially a Swarm A versus Swarm C comparison.

999 In contrast to Comparison X, here we see two FAC replications that, though vary-
 1000 ing somewhat, are structurally very similar. The southernmost return current sheets for
 1001 both Simulations XIa – b are similar in strength, width, and location, as is shown by the
 1002 red flux tubes who capture around 1.2 kA in the same place for both simulations. The
 1003 return current sheet just above, captured by the green flux tubes, is around half as strong
 1004 in Simulation XIb and positioned ~ 7 km southward, and the orange flux tubes carry a
 1005 similar 1.5 – 1.6 kA of Hall current at nearly the same location in both simulations. Over-
 1006 all, Comparison XI provides support for the extrapolation of FAC data over a distance
 1007 of around 50 km, ~~up to the differences in auroral arc simulations seen here.~~

1008 **4.3.3 Summary: Along-Arc FAC Structure**

1009 Two of our six conjunction events benefit from being able to use a second data track
 1010 in their replications and subsequent simulations. Comparisons X and XI show to what
 1011 extent the FAC map can change in just under 50 km, providing important insight into
 1012 the confidence of all of our FAC replications, and consequently the resulting 3-D sim-
 1013 ulations of these auroral arc systems. Overall, contingent on the morphology indicated
 1014 by the imagery and aside from minor FAC signatures, replicating the FAC data using
 1015 arc boundaries defined by auroral imagery is a justifiable method for creating 2-D, con-
 1016 tinuous driver maps for 3-D simulations of auroral arc systems.

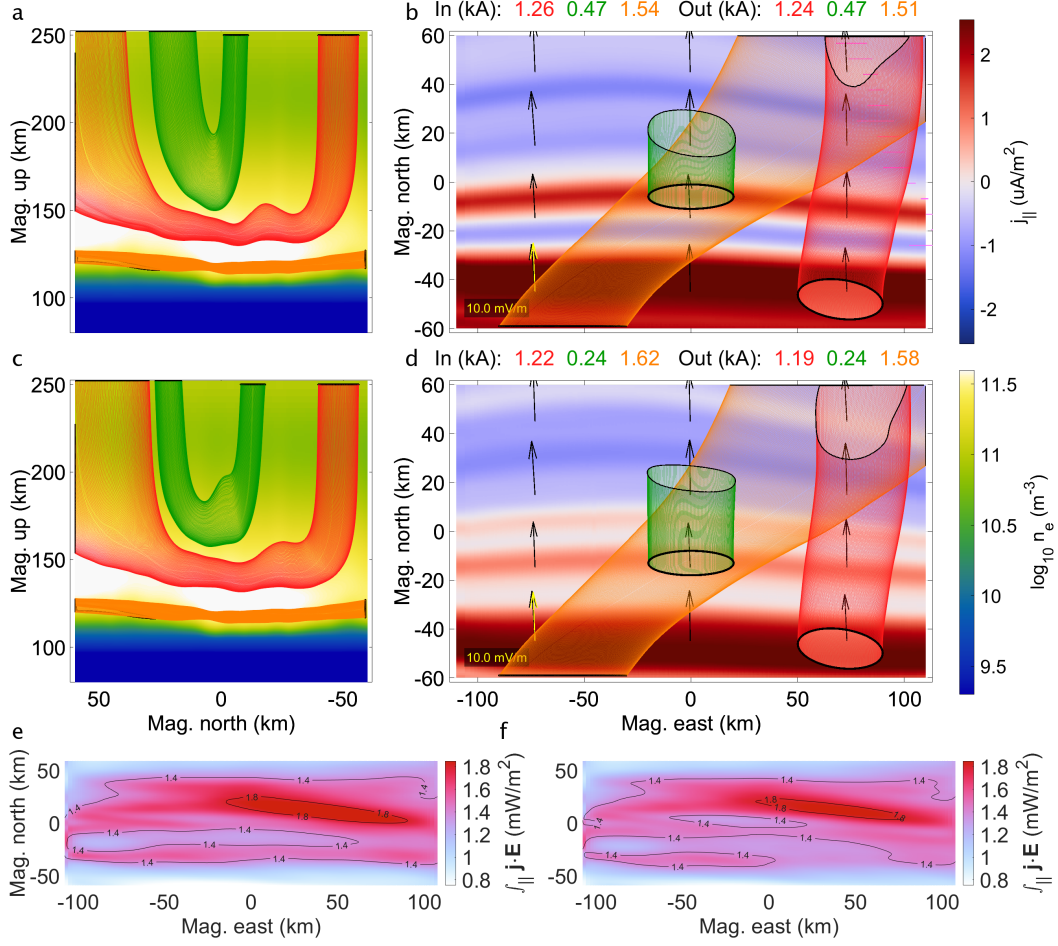


Figure 16. Comparison XI (March 14, 6:49 UT): Top and side views of Simulation XIa with a FAC replication using both Swarm A (east) and C (west) (a, b) versus Simulation XIb with a FAC replication using only Swarm A (c, d) along with height-integrated Joule heating for Simulation XIa (e) and XIb (f). For plot details, see Section 2.8. Data sources: Swarm (2025), SuperDARN (2025), and van Irsel, J. (2025).

1017 5 Discussions & Conclusions

1018 Current closure morphology and Joule heating from resulting closure currents are
 1019 two important aspects of ionospheric physics, particularly surrounding discrete auroral
 1020 arc systems. By carefully incorporating observational data from multi-instrument con-
 1021 junctions into input drivers of auroral arc simulations, we point out three aspects that
 1022 the results are susceptible to: (1) the along-arc structure in FAC and the arc-boundary replica-
 1023 tion technique, (2) the constant background flow, and (3) the specifics of electron precipitation. (1) the
 1024 constant background flow, (2) the specifics of electron precipitation, and (3) the along-
 1025 arc structure in FAC and the arc-boundary replication technique. Here, we conclude
 1026 our findings and discuss possible future studies that can advance from this work.

1027 Auroral arc systems should be studied in three dimensions to fully understand field-
 1028 aligned current closure and, by extension, Magnetosphere-Ionosphere-Thermosphere cou-
 1029 pling. We show, using several permutations of 3-D, electrostatic, data-driven, auroral
 1030 arc simulations across six conjunction events, that flux tubes of electric current navigate
 1031 around one another in their closure paths; something they cannot do in height-integrated
 1032 (east, north), or cross-arc (north-up) two-dimensional descriptions. These current flux
 1033 tubes tell the story of how FAC, ionospheric electric fields, and Pedersen and Hall con-
 1034 ductivities interplay in a cohesive, self-consistent manner, and they do so with more de-
 1035 tail than 2-D descriptions allow.

1036 To produce top-boundary driver maps for our simulations, we demonstrate the use
 1037 of auroral-imagery-guided FAC replication, similar to methods outlined by Clayton et
 1038 al. (2019); van Irsel et al. (2024). We show that this method can produce FAC maps that
 1039 are geophysically consistent with maps of precipitation energetics, and that hold reason-
 1040 ably well for major arc-scale FAC structure. However, more minor FAC structure may
 1041 appear or disappear when moving in the along-arc direction over distances on the order
 1042 of 50 km. Along-arc variations below this scale size may well exist, but these are beyond
 1043 the scope of this work given that we are limited by the 50 km Swarm spacecraft separa-
 1044 tion. Even so, this methodology uses maximal information from imagery derived precip-
 1045 itation maps to provide geophysically meaningful extrapolations of FAC surrounding au-
 1046 roral arcs.

1047 The 3-D auroral arc simulations covered in this paper have been shown to be very
 1048 sensitive to both the magnitude and the direction of the constant, large-scale, background
 1049 electric field, $\bar{\mathbf{E}}$. Equation 2 shows what the choice of $\bar{\mathbf{E}}$ implies about the 2-D top-boundary
 1050 FAC driver map, and thus, how the simulations interpret these maps. We draw the fol-
 1051 lowing conclusions about how $\bar{\mathbf{E}}$, in the absence of neutral winds, affects discrete auro-
 1052 ral arc systems:

- 1053 • Strong background convection fields can render the use of Hall currents in FAC
 1054 closure negligible, while weak background convection fields put emphasis on both
 1055 local polarization fields and FAC closure through the electrojet.
- 1056 • Across-arc electric fields provide shorter closure paths making FAC close through
 1057 Pedersen current more often.
- 1058 • FAC sheets close with adjacent ones only in the direction of the electric field.
- 1059 • When part of the electric field is directed along the arc, it lengthens the closure
 1060 paths and, as current flux tubes cannot intersect, it pushes additional tubes to Hall
 1061 current altitudes.
- 1062 • The manner in which the background electric field affects current connectivity, along
 1063 with the electric field itself, significantly alters Joule heating, and thus the elec-
 1064 trostatic load characteristics, of auroral arc systems.

1065 These conclusions support the idea that large-scale convection flow conditions are a dom-
 1066 inant driver of the specific morphology of auroral arc systems, with which the arc-scale
 1067 ionosphere perturbs \mathbf{E} in accordance with a 3-D conductivity volume.

1068 In addition to background convection fields, auroral arc systems are also sensitive
 1069 to the specifics of precipitating electron energy distributions. We show that the use of
 1070 unaccelerated Maxwellian spectra can erroneously enhance impact ionization at lower
 1071 altitudes, resulting in an overestimation of E -region densities. We compare the use of
 1072 such spectra against accelerated Maxwellian spectra, which decouple the peak energy
 1073 from the energy spread. Even for simulations whose source region characteristic energy
 1074 is estimated to be relatively large, $T_s \sim 800$ eV, the unaccelerated assumption still greatly
 1075 overestimates density enhancements at lower altitudes. We show the following:

- 1076 • [The availability of multi-spectral, rather than white-light, all-sky imagery allows](#)
 1077 [the community to move away from the assumption of unaccelerated Maxwellian](#)
 1078 [precipitation spectra, and toward energy distributions which decouple the energy](#)
 1079 [spread from the peak energy, allowing for more flexibility in modeling electron](#)
 1080 [precipitation.](#)
- 1081 • The choice of accelerated versus unaccelerated Maxwellian electron precipitation
 1082 most affects FAC closure in auroral arc systems when the Hall currents play a con-
 1083 siderable role in this closure.
- 1084 • Keeping FAC and total precipitating electron energy drivers constant, the choice
 1085 of unaccelerated over accelerated precipitation alone can increase the calculated
 1086 height-integrated Joule heating by 30 – 50 % in some auroral arc systems.
- 1087 • Unaccelerated Maxwellian auroral precipitation assumptions can greatly enhance
 1088 electrojet currents compared to accelerated precipitation assumptions.

1089 This work looks at how to determine geophysical, self-consistent solutions to cur-
 1090 rent continuity in auroral arc systems, and what these systems are sensitive to, thus un-
 1091 covering how important various parameters can be. How then do we know which solu-
 1092 tion is correct? The existence of TII ion drift data (or other, independent ~~flow data~~[data](#)
 1093 [such as those from the Electrojet Zeeman Imaging Explorer mission](#) (Madelaine et al.,
 1094 2023)) from the Swarm spacecraft invites comparisons to the calculated GEMINI out-
 1095 put flow maps covered in this paper. Figure 17 shows two such comparisons of the mag-
 1096 netic eastward TII flow (assuming no along-track component) across the model space for
 1097 two of the simulations (Ib and IVb). While we have generated 17 simulations of the six
 1098 events in Table 1, only the February 10 and March 14 conjunctions include Swarm A TII
 1099 data; only the former has the crossing directly within the model space. The simulations
 1100 using PFISR for the background flow for these two cases match better than the corre-
 1101 sponding SuperDARN runs, which have smaller background flows.

1102 It is notable among the examples chosen for this study (the six events in Table 1)
 1103 that there is not a particularly strong correlation between the magnetic and electric field
 1104 signatures in the raw Swarm data—for most of these events, the $\nabla \cdot \mathbf{E}$ term in Equa-
 1105 tion 1 is apparently not the major player for the events in Table 1 ([except for perhaps](#)
 1106 [Simulation IIIb](#)). Thus this comparison with TII becomes mostly a question of match-
 1107 ing the background flow to the TII value, perhaps why the nearer source (PFISR) pro-
 1108 vides the closest match. For the first example shown, there are some $\nabla \cdot \mathbf{E}$ signatures
 1109 in both TII and the GEMINI results, but the GEMINI result is somewhat smoother and
 1110 slightly offset. Both of these differences may well be artifacts of the image inversion pro-
 1111 cess.

1112 Finally we can consider whether the competition between the $\nabla \cdot \mathbf{E}$ and $\nabla \Sigma_{P,H}$
 1113 terms in Equation 1 provides a truly unique solution to the problem posed. There is a
 1114 strong dependence on the chosen $\bar{\mathbf{E}}$: choosing the background electric field differently
 1115 finds different situations. There may be choices, beyond what PFISR and SuperDARN

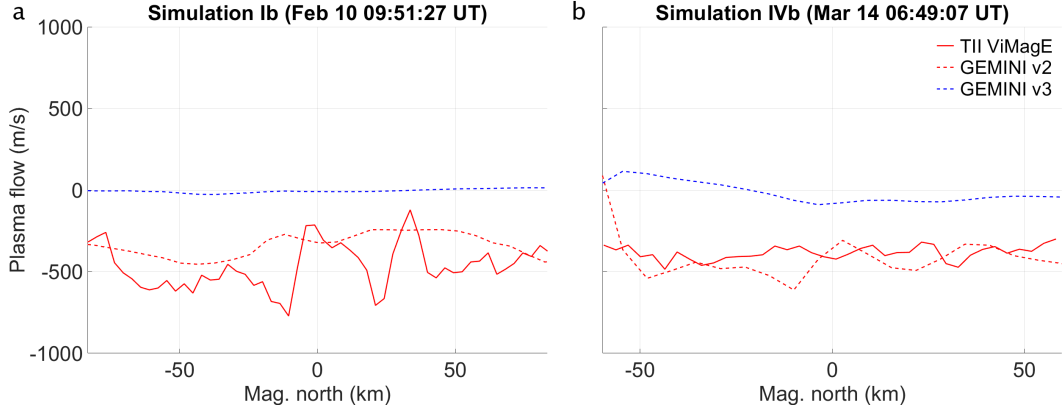


Figure 17. GEMINI versus TII flow comparisons for Simulations Ib (a) and IVb (b). The GEMINI magnetic eastward, “v2”, and northward, “v3”, plasma flows are interpolated through the simulation volume at the Swarm A tracks. TII magnetic eastward ion drift data, “ViMagE”, are converted to geomagnetic coordinates assuming no along-track component. Both simulations use PFISR derived background flow, accelerated Maxwellian precipitation, and double-spacecraft replications. Data sources: Swarm (2025), PFISR (2025), and van Irsel, J. (2025).

1116 provide, which more closely track the TII cross-track flow values. We do see that choos-
 1117 ing different background flows, e.g. the no-background flow run versus the large-background
 1118 flow simulations in Comparison III, generates in the GEMINI result a visible $\nabla \cdot \mathbf{E}$ sig-
 1119 nature which, though still there, is masked when the imposed background electric field
 1120 is strengthened. Future work exploring these comparisons with TII should include (a)
 1121 events like the one covered by Clayton et al. (2021), with its strong $\nabla \cdot \mathbf{E}$ signature; and
 1122 (b) further study of error sources stemming from matching the spacecraft data to inverted
 1123 imagery, particularly for oblique camera angles which tend to blur and misplace discrete
 1124 arc structures. We also note the scale of smoothing applied for these runs, as described
 1125 in Subsections 2.1 and 2.2: this level of smoothing may yet be hiding relevant physics,
 1126 particularly at sharp arc edge boundaries.

1127 The tools developed herein provide a means for data-driven event case study sim-
 1128 ulations to be routinely done, assuming sufficient data coverage. Upcoming iterations
 1129 may consider different, incomplete combinations of input and/or adaptation of our meth-
 1130 ods into a formal physics-based assimilation scheme. A subject for further studies is the
 1131 investigation of the sensitivity to other simulation choices made, such as data smooth-
 1132 ing, conductance isocontours, etc. Also, the relevant physical gradient limit caused by
 1133 recombination and collisions in the current closure altitude region: how sharp of gradi-
 1134 ents can be sustained and be relevant?

1135 In the collective effort to try and understand the nature of aurorae, the instruments
 1136 that provide our observational data are an ever-existing limitation. It would be optimal
 1137 to deploy 1000s of spacecraft, radars, and imagers across the northern and southern aur-
 1138 oral ovals (Nykyri et al., 2025), but this is impractical. Hence, measurements must be
 1139 targeted and focused on parameters that are most influential to the physics at hand. This
 1140 work provides three such aspects to contribute to this focus and aids in making decisions
 1141 as to what is important and when.

1142 **Appendix A Derivation of Accelerated Bi-Maxwellian Differential Num-**
 1143 **ber Flux**

1144 In order to implement the impact ionization calculations by Fang et al. (2010), we
 1145 need the differential (as a function of energy) hemispherical number flux, i.e. electrons/eV/s/cm²,
 1146 of precipitating energetic auroral electrons at the topside of the ionosphere for every latitude-
 1147 longitude pair. To derive this flux for an accelerated population we start with a bi-Maxwellian
 1148 source at the plasmashet as is done by Fridman and Lemaire (1980):

$$g_s(v_{\parallel,s}, v_{\perp,s}, \varphi) d^3v = n_{e,s} \left(\frac{m_e}{2\pi}\right)^{3/2} \frac{1}{E_{\parallel,s}^{1/2} E_{\perp,s}} \exp\left[-\frac{m_e v_{\parallel,s}^2}{2E_{\parallel,s}} - \frac{m_e v_{\perp,s}^2}{2E_{\perp,s}}\right] v_{\perp,s} dv_{\parallel} dv_{\perp} d\varphi, \quad (\text{A1})$$

1149 where $n_{e,s}$ is the source region electron density, m_e is the mass of an electron, $E_{\parallel,s}$ and
 1150 $E_{\perp,s}$ are the parallel and perpendicular characteristic energies, $v_{\parallel,s}$ and $v_{\perp,s}$ are the source
 1151 region parallel and perpendicular speeds, and φ is the azimuthal coordinate. As electrons
 1152 precipitate down towards the ionosphere they undergo no collisions—their velocities change
 1153 in two ways only (Knight, 1973; Fridman & Lemaire, 1980; Kaeppler, 2013):

- 1154 1. The conservation of the first adiabatic invariant, i.e. the mirror force, increases
 1155 their perpendicular velocity:

$$v_{\perp,s} = \frac{1}{\sqrt{\beta}} v_{\perp,i}, \quad (\text{A2})$$

1156 where $\beta = B_i/B_s > 1$, and B_i and B_s are the ionospheric and source region
 1157 magnetic field strengths.

- 1158 2. The conservation of energy increases the square magnitude speed as they fall through
 1159 the parallel potential difference, U_a :

$$v_{\parallel,i}^2 + v_{\perp,i}^2 = v_{\parallel,s}^2 + v_{\perp,s}^2 + \frac{2U_a}{m_e}. \quad (\text{A3})$$

1160 This provides the parallel source region speed as a function of the ionospheric coordi-
 1161 nates:

$$v_{\parallel,s} = \pm \sqrt{v_{\parallel,i}^2 + v_{\perp,i}^2 \frac{\beta - 1}{\beta} - \frac{2U_a}{m_e}}. \quad (\text{A4})$$

1162 From here, we use Liouville's theorem which tells us that, along a well-defined path through
 1163 phase space, e.g. $(\mathbf{x}, \mathbf{v})_s \rightarrow (\mathbf{x}, \mathbf{v})_i$, the phase space density is held constant such that

$$g_i(\mathbf{x}_i, \mathbf{v}_i) = g_s(\mathbf{x}_s, \mathbf{v}_s). \quad (\text{A5})$$

1164 A good assumption is to say that we may separate spatial and velocity coordinates, $g(\mathbf{x}, \mathbf{v}) =$
 1165 $n(\mathbf{x})f(\mathbf{v})$, and that locally the densities are constants, i.e. $n_i(\mathbf{x}) = n_{e,i}$, $n_s(\mathbf{x}) = n_{e,s}$.

1166 This tells us

$$g_i(\mathbf{v}_i) = g_s(\mathbf{v}_s) = g_s(\mathbf{v}_s(\mathbf{v}_i)), \quad (\text{A6})$$

1167 such that

$$g_i(v_{\parallel,i}, v_{\perp,i}) d^2v = n_{e,s} \frac{m_e^{3/2}/\sqrt{2\pi}}{E_{\parallel,s}^{1/2} E_{\perp,s}} \exp\left[-\frac{m_e \left(v_{\parallel,i}^2 + v_{\perp,i}^2 \frac{\beta-1}{\beta} - \frac{2U_a}{m_e}\right)}{2E_{\parallel,s}} - \frac{m_e v_{\perp,i}^2/\beta}{2E_{\perp,s}}\right] \frac{v_{\perp,i}}{\sqrt{\beta}} dv_{\parallel} dv_{\perp} \quad (\text{A7})$$

1168 where we've integrated over φ . The ionospheric density is thus

$$n_{e,i} = n_{e,s} \frac{E_{\parallel,s} \sqrt{\beta}}{E_{\parallel,s} + E_{\perp,s}(\beta - 1)} \exp\left[\frac{U_a}{E_{\parallel,s}}\right]. \quad (\text{A8})$$

1169 Note that $U_a \rightarrow 0$ and $E_{\parallel,s} \rightarrow E_{\perp,s}$ gives a familiar density relation: $n_{e,i} = n_{e,s}/\sqrt{\beta}$.
 1170 Now that we have the velocity distribution function at the ionosphere, we find the dif-
 1171 ferential number flux using $J_{\parallel,i}(\mathbf{v}_i) d^3v = v_{\parallel,i} g_i(\mathbf{v}_i) d^3v$ and then we perform the fol-
 1172 lowing change of coordinates:

$$v_{\parallel,i} = v \cos \theta = \sqrt{2E/m_e} \cos \theta \quad \text{and} \quad v_{\perp,i} = v \sin \theta = \sqrt{2E/m_e} \sin \theta, \quad (\text{A9})$$

with θ being the pitch angle, and with Jacobian determinant $1/m_e$. The energy, E , has the condition

$$E = \frac{m_e}{2} (v_{\parallel,i}^2 + v_{\perp,i}^2) \geq U_a, \quad (\text{A10})$$

as per Equation A3. This gives

$$J_{\parallel,i}(E, \theta) dE d\theta = \frac{n_{e,s}}{\sqrt{m_e}} \frac{1}{E_{\parallel,s}^{1/2} E_{\perp,s}} \frac{\sin 2\theta}{\sqrt{2\pi\beta}} E \exp \left[-\frac{E - U_a}{E_{\parallel,s}} - \left(\frac{E}{E_{\perp,s}} - \frac{E}{E_{\parallel,s}} \right) \frac{\sin^2 \theta}{\beta} \right] dE d\theta. \quad (\text{A11})$$

With unit-less parameters $\varepsilon \equiv E/E_{\parallel,s}$, $u_a \equiv U_a/E_{\parallel,s}$, and $\delta \equiv E_{\perp,s}/E_{\parallel,s}$, we get

$$\frac{1}{n_{e,s}} \sqrt{\frac{m_e}{E_{\parallel,s}}} J_{\parallel,i}(E, \theta) dE d\theta = \frac{\sin 2\theta}{\sqrt{2\pi\beta}} \frac{\varepsilon}{\delta} \exp \left[-(\varepsilon - u_a) - \left(\frac{\varepsilon}{\delta} - \varepsilon \right) \frac{\sin^2 \theta}{\beta} \right] d\varepsilon d\theta. \quad (\text{A12})$$

We now integrate over $v_{\parallel,i} > 0$, i.e. $0 \leq \theta \leq \pi/2$, and find the hemispherical differential number flux.

$$J_{\parallel,i}(\varepsilon) d\varepsilon = n_{e,s} \sqrt{\frac{E_{\parallel,s}}{m_e}} \frac{1}{\delta \sqrt{2\pi\beta}} G \left(\frac{\delta - 1}{\delta\beta} \varepsilon \right) \varepsilon e^{-\varepsilon + u_a} d\varepsilon, \quad \text{where } G(x) \equiv \frac{e^x - 1}{x}. \quad (\text{A13})$$

For similar parallel and perpendicular source temperatures, we have $\delta \sim 1$, and we have $\beta \sim 10^3$ for a plasmashet source region (Fridman & Lemaire, 1980), where $G(x \ll 1) \rightarrow 1 + x/2 + \mathcal{O}(x^2)$ such that

$$J_{\parallel,i}(\varepsilon) d\varepsilon \approx n_{e,s} \sqrt{\frac{E_{\parallel,s}}{m_e}} \frac{1}{\delta \sqrt{2\pi\beta}} \left(1 + \frac{\delta - 1}{2\delta\beta} \varepsilon \right) \varepsilon e^{-\varepsilon + u_a} d\varepsilon \quad (\text{A14})$$

If we re-cast this in terms of normalized total precipitating energy flux, $q_p \equiv Q_p/E_{\parallel,s}$, where

$$q_p = \int_{u_a}^{\infty} \varepsilon J_{\parallel,i}(\varepsilon) d\varepsilon, \quad (\text{A15})$$

we get

$$J_{\parallel,i}(\varepsilon) d\varepsilon = q_p \frac{1 + \chi\varepsilon}{2 + 6\chi + u_a(2 + u_a + (6 + u_a(3 + u_a))\chi)} \varepsilon e^{-\varepsilon + u_a} d\varepsilon, \quad \text{where } \chi = \frac{\delta - 1}{2\delta\beta}. \quad (\text{A16})$$

We note that in our regime of $\beta \sim 10^3$ we may ignore the temperature difference at the source, so if we take the limit of $\delta \rightarrow 1$ we get a familiar result

$$J_{\parallel,i}(E) dE = \frac{Q_p}{T_s^2 + (T_s + U_a)^2} \frac{E}{T_s} \exp \left[-\frac{E - U_a}{T_s} \right] dE, \quad E \geq U_a \quad (\text{A17})$$

where, for clarity, we have defined $T_s \equiv E_{\parallel,s}$. These results have been congregated from knowledge and derivations obtained in publications by Medicus (1961); Evans (1974); Fridman and Lemaire (1980); Strickland et al. (1989); Kaeppler (2013).

Open Research Section

All 3-D simulation data, imagery inversions, and supporting metadata are available at <https://rcweb.dartmouth.edu/LynchK>. The data for the Poker Flat DASC are available at <http://optics.gi.alaska.edu/optics/archive>, for AMISR at <https://data.amisr.com/database>, for SuperDARN at <https://superdarn.ca/data-download>, and for the Swarm at <https://swarm-diss.eo.esa.int>. The GEMINI source code and documentation is available at <https://github.com/gemini3d> and the replication/visualization tools at https://github.com/317Lab/aurora_gemini.

Acknowledgments

We thank NASA for funding Jules van Irsel from Grant 80NSSC23K1622 through the FINESST program and Dartmouth College for providing internal funding for Phase A

1201 of the Auroral Reconstruction CubeSwarm proposal from which a lot of this research stems,
 1202 and we acknowledge NASA Grant 80GSFC21C0009 for the ARCS MIDEX CSR fund-
 1203 ing. AMISR facilities, including PFISR, are operated and maintained for the US National
 1204 Science Foundation (NSF) by SRI International under a cooperative agreement #AGS-
 1205 1840962. AMISR data are produced and made publicly available for scientific and aca-
 1206 demic research purposes under the same award. This work uses version 0302, level 1B
 1207 data from the Thermal Ion Imagers and version 0401, level 2 FAC data made possible
 1208 by the European Space Agency’s Swarm Data, Innovation, and Science Cluster and Cana-
 1209 dian Space Agency grant 15 SUSWARM. We thank NASA for providing funding for the
 1210 GEMINI model development from Grant 80NSSC24K0126. 3-D simulations supporting
 1211 this work were facilitated by the Discovery cluster at Dartmouth Research Computing
 1212 and the NASA High-End Computing (HEC) Program through the NASA Advanced Su-
 1213 percomputing (NAS) Division at Ames Research Center. The authors acknowledge the
 1214 use of SuperDARN data and thank Daniel Billett for collecting SuperDARN convection
 1215 flow data for use in this paper. SuperDARN is a collection of radars funded by national
 1216 scientific funding agencies of Australia, Canada, China, France, Italy, Japan, Norway,
 1217 South Africa, United Kingdom and the United States of America. We thank Michael Hirsch,
 1218 Terry Kovacs, and John Griffin for GEMINI and computational technical support.

1219 References

- 1220 Amm, O., Aruliah, A., Buchert, S. C., Fujii, R., Gjerloev, J. W., Ieda, A., ...
 1221 Yoshikawa, A. (2008). Towards understanding the electrodynamics of the
 1222 3-dimensional high-latitude ionosphere: Present and future. *Annales Geophysi-*
 1223 *caae*, *26*(12), 3913–3932. doi: 10.5194/angeo-26-3913-2008
- 1224 Amm, O., Fujii, R., Kauristie, K., Aikio, A., Yoshikawa, A., Ieda, A., & Vanhamäki,
 1225 H. (2011). A statistical investigation of the Cowling channel efficiency in the
 1226 auroral zone. *Journal of Geophysical Research: Space Physics*, *116*(A2). doi:
 1227 10.1029/2010JA015988
- 1228 Burchill, J. K., & Knudsen, D. J. (2022). Swarm Thermal Ion Imager measurement
 1229 performance. *Earth, Planets and Space*, *74*(1), 181. doi: 10.1186/s40623-022-
 1230 -01736-w
- 1231 Clayton, R., Burleigh, M., Lynch, K. A., Zettergren, M., Evans, T., Grubbs, G.,
 1232 ... Varney, R. (2021). Examining the auroral ionosphere in three dimen-
 1233 sions using reconstructed 2D maps of auroral data to drive the 3D GEM-
 1234 INI model. *Journal of Geophysical Research: Space Physics*, *126*(11). doi:
 1235 10.1029/2021JA029749
- 1236 Clayton, R., Lynch, K., Zettergren, M., Burleigh, M., Conde, M., Grubbs, G., ...
 1237 Varney, R. (2019). Two-dimensional maps of in situ ionospheric plasma flow
 1238 data near auroral arcs using auroral imagery. *Journal of Geophysical Research:*
 1239 *Space Physics*, *124*(4), 3036–3056. doi: 10.1029/2018JA026440
- 1240 Conde, M., Craven, J. D., Immel, T., Hoch, E., Stenbaek-Nielsen, H., Hallinan, T.,
 1241 ... Sigwarth, J. (2001). Assimilated observations of thermospheric winds, the
 1242 aurora, and ionospheric currents over Alaska. *Journal of Geophysical Research:*
 1243 *Space Physics*, *106*(A6), 10493–10508. doi: 10.1029/2000JA000135
- 1244 Cowley, S. W. H. (2000). Magnetosphere-ionosphere interactions: A tutorial review.
 1245 *Magnetospheric Current Systems, Geophysical Monograph Series*, *118*, 91–106.
- 1246 Cowling, T. G. (1932). The electrical conductivity of an ionised gas in the presence
 1247 of a magnetic field. *Monthly Notices of the Royal Astronomical Society*, *93*(1),
 1248 90–97. doi: 10.1093/mnras/93.1.90
- 1249 DASC. (2025). <ftp://optics.gi.alaska.edu/GAK/DASC>.
- 1250 Enengl, F., Kotova, D., Jin, Y., Clausen, L. B. N., & Miloch, W. J. (2023). Iono-
 1251 spheric plasma structuring in relation to auroral particle precipitation. *Journal*
 1252 *of Space Weather and Space Climate*, *13*. doi: 10.1051/swsc/2022038
- 1253 Evans, D. S. (1968). The observations of a near monoenergetic flux of auroral elec-

- 1254 trons. *Journal of Geophysical Research (1896–1977)*, *73*(7), 2315–2323. doi: 10
 1255 .1029/JA073i007p02315
- 1256 Evans, D. S. (1974). Precipitating electron fluxes formed by a magnetic field aligned
 1257 potential difference. *Journal of Geophysical Research*, *79*(19), 2853–2858. doi:
 1258 10.1029/JA079i019p02853
- 1259 Fang, X., Randall, C. E., Lummerzheim, D., Solomon, S. C., Mills, M. J., Marsh,
 1260 D. R., ... Lu, G. (2008). Electron impact ionization: A new parameteriza-
 1261 tion for 100 eV to 1 MeV electrons. *Journal of Geophysical Research: Space*
 1262 *Physics*, *113*(A9). doi: 10.1029/2008JA013384
- 1263 Fang, X., Randall, C. E., Lummerzheim, D., Wang, W., Lu, G., Solomon, S. C., &
 1264 Frahm, R. A. (2010). Parameterization of monoenergetic electron impact
 1265 ionization. *Geophysical Research Letters*, *37*(22). doi: 10.1029/2010GL045406
- 1266 Farley Jr., D. T. (1959). A theory of electrostatic fields in a horizontally strati-
 1267 fied ionosphere subject to a vertical magnetic field. *Journal of Geophysical Re-*
 1268 *search (1896–1977)*, *64*(9), 1225–1233. doi: 10.1029/JZ064i009p01225
- 1269 Fridman, M., & Lemaire, J. (1980). Relationship between auroral electrons fluxes
 1270 and field aligned electric potential difference. *Journal of Geophysical Research:*
 1271 *Space Physics*, *85*(A2), 664–670. doi: 10.1029/JA085iA02p00664
- 1272 Fujii, R., Amm, O., Vanhamäki, H., Yoshikawa, A., & Ieda, A. (2012). An appli-
 1273 cation of the finite length Cowling channel model to auroral arcs with longi-
 1274 tudinal variations. *Journal of Geophysical Research: Space Physics*, *117*. doi:
 1275 10.1029/2012JA017953
- 1276 Fujii, R., Amm, O., Yoshikawa, A., Ieda, A., & Vanhamäki, H. (2011). Reformula-
 1277 tion and energy flow of the Cowling channel. *Journal of Geophysical Research:*
 1278 *Space Physics*, *116*(A2). doi: 10.1029/2010JA015989
- 1279 Greenwald, R. A., Baker, K. B., Dudeney, J. R., Pinnock, M., Jones, T. B., Thomas,
 1280 E. C., ... Yamagishi, H. (1995, Feb 01). DARN/SuperDARN. *Space Science*
 1281 *Reviews*, *71*(1), 761–796. doi: 10.1007/BF00751350
- 1282 Grubbs II, G., Michell, R., Samara, M., Hampton, D., Hecht, J., Solomon, S., &
 1283 Jahn, J. (2018). A comparative study of spectral auroral intensity predictions
 1284 from multiple electron transport models. *Journal of Geophysical Research:*
 1285 *Space Physics*, *123*(1), 993–1005. doi: 10.1002/2017JA025026
- 1286 Grubbs II, G., Michell, R., Samara, M., Hampton, D., & Jahn, J. (2018). Pre-
 1287 dicting electron population characteristics in 2-D using multispectral
 1288 ground-based imaging. *Geophysical Research Letters*, *45*(1), 15–20. doi:
 1289 10.1002/2017GL075873
- 1290 Hecht, J., Strickland, D., & Conde, M. (2006). The application of ground-based
 1291 optical techniques for inferring electron energy deposition and composition
 1292 change during auroral precipitation events. *Journal of Atmospheric and Solar-*
 1293 *Terrestrial Physics*, *68*(13), 1501–1519. doi: 10.1016/j.jastp.2005.06.022
- 1294 Heinselman, C. J., & Nicolls, M. J. (2008). A Bayesian approach to electric field
 1295 and E-region neutral wind estimation with the Poker Flat Advanced Modular
 1296 Incoherent Scatter Radar. *Radio Science*, *43*(5). doi: 10.1029/2007RS003805
- 1297 Imajo, S., Miyoshi, Y., Kazama, Y., Asamura, K., Shinohara, I., Shiokawa, K.,
 1298 ... Hori, T. (2024). Precipitation of auroral electrons accelerated at very
 1299 high altitudes: Impact on the ionosphere and a possible acceleration mech-
 1300 anism. *Journal of Geophysical Research: Space Physics*, *129*(9). doi:
 1301 10.1029/2024JA032696
- 1302 Janhunen, P. (2001). Reconstruction of electron precipitation characteristics from
 1303 a set of multiwavelength digital all-sky auroral images. *Journal of Geophysical*
 1304 *Research: Space Physics*, *106*(A9), 18505–18516. doi: 10.1029/2000JA000263
- 1305 Kaeppeler, S. R. (2013). *A rocket-borne investigation of auroral electrodynamics*
 1306 *within the auroral-ionosphere* (Unpublished doctoral dissertation). University
 1307 of Iowa.
- 1308 Kaeppeler, S. R., Kletzing, C. A., Rowland, D. E., Jones, S., Heinselman, C. J.,

- 1309 Bounds, S. R., ... Pfaff, R. F. (2012). *Current closure in the auroral iono-*
 1310 *sphere: Results from the auroral current and electrodynamic structure rocket*
 1311 *mission*. Hampton, VA: NASA/Langley Research Center.
- 1312 Karlsson, T., Andersson, L., Gillies, D., Lynch, K., Marghitu, O., Partamies, N.,
 1313 ... Wu, J. (2020). Quiet, discrete auroral arcs-observations. *Space Science*
 1314 *Reviews*, 216(1), 1–50.
- 1315 Kelley, M. C. (2009). *The Earth's ionosphere: Plasma physics and electrodynamic*
 1316 *(2nd ed.)*. Amsterdam, Netherlands: Academic Press.
- 1317 Kelly, J., & Heinselman, C. (2009). Initial results from Poker Flat Incoherent Scatter
 1318 Radar (PFISR). *Journal of Atmospheric and Solar-Terrestrial Physics*, 71(6),
 1319 635. doi: 10.1016/j.jastp.2009.01.009
- 1320 Khazanov, G. V., Robinson, R. M., Zesta, E., Sibeck, D. G., Chu, M., & Grubbs,
 1321 G. A. (2018). Impact of precipitating electrons and magnetosphere-ionosphere
 1322 coupling processes on ionospheric conductance. *Space Weather*, 16(7), 829–837.
 1323 doi: 10.1029/2018SW001837
- 1324 Knight, S. (1973). Parallel electric fields. *Planetary and Space Science*, 21(5),
 1325 741–750. doi: 10.1016/0032-0633(73)90093-7
- 1326 Knudsen, D. J., Burchill, J. K., Buchert, S. C., Eriksson, A. I., Gill, R., Wahlund,
 1327 J.-E., ... Moffat, B. (2017). Thermal ion imagers and Langmuir probes in
 1328 the Swarm electric field instruments. *Journal of Geophysical Research: Space*
 1329 *Physics*, 122(2), 2655–2673. doi: 10.1002/2016JA022571
- 1330 Lamarche, L., & Reimer, A. (2025). <https://zenodo.org/records/10892410>.
- 1331 Laundal, K. M., & Richmond, A. D. (2017, 3 1). Magnetic coordinate systems.
 1332 *Space Science Reviews*, 206(1), 27–59. doi: 10.1007/s11214-016-0275-y
- 1333 Lotko, W. (2004). Inductive magnetosphere-ionosphere coupling. *Journal of Atmo-*
 1334 *spheric and Solar-Terrestrial Physics*, 66(15), 1443–1456. doi: 10.1016/j.jastp
 1335 .2004.03.027
- 1336 Lynch, K. A., McManus, E., Gutow, J., Burleigh, M., & Zettergren, M. (2022). An
 1337 ionospheric conductance gradient driver for subauroral picket fence visible sig-
 1338 natures near STEVE events. *Journal of Geophysical Research: Space Physics*,
 1339 127(12). doi: 10.1029/2022JA030863
- 1340 Madelaire, M., Laundal, K., Gjerloev, J., Hatch, S., Reistad, J., Vanhamäki, H.,
 1341 ... Merkin, V. (2023). Spatial resolution in inverse problems: The EZIE
 1342 satellite mission. *Journal of Geophysical Research: Space Physics*, 128(5),
 1343 e2023JA031394. doi: 10.1029/2023JA031394
- 1344 Mallinckrodt, A. J. (1985). A numerical simulation of auroral ionospheric electrody-
 1345 namics. *Journal of Geophysical Research: Space Physics*, 90(A1), 409–417. doi:
 1346 10.1029/JA090iA01p00409
- 1347 Marghitu, O. (2012). Auroral arc electrodynamic: Review and outlook. In *Auroral*
 1348 *phenomenology and magnetospheric processes: Earth and other planets* (pp.
 1349 143–158). American Geophysical Union (AGU). doi: 10.1029/2011GM001189
- 1350 Marghitu, O., Klecker, B., & McFadden, J. P. (2006). The anisotropy of precipitat-
 1351 ing auroral electrons: A FAST case study. *Advances in Space Research*, 38(8),
 1352 1694–1701. (Magnetospheric dynamics and the international living with a star
 1353 program) doi: 10.1016/j.asr.2006.03.028
- 1354 Medicus, G. (1961, 12). Theory of electron collection of spherical probes. *Journal of*
 1355 *Applied Physics*, 32(12), 2512–2520. doi: 10.1063/1.1728342
- 1356 Mule, A. (2025). <https://github.com/317Lab/asispectralinversion>.
- 1357 Nicolls, M. J., & Heinselman, C. J. (2007). Three-dimensional measurements of trav-
 1358 eling ionospheric disturbances with the Poker Flat Incoherent Scatter Radar.
 1359 *Geophysical Research Letters*, 34(21). doi: 10.1029/2007GL031506
- 1360 Nykyri, K., Blanco-Cano, X., Knudsen, D., Sibeck, D. G., & Borovsky, J. E. (2025).
 1361 Editorial: Past, present and future of multispacecraft measurements for space
 1362 physics. *Frontiers in Astronomy and Space Sciences*, December 2025. doi:
 1363 10.3389/fspas.2025.1579994

- 1364 Paschmann, G., Haaland, S., & Treumann, R. (2003). *Auroral plasma physics*. Dor-
 1365 drecht, Netherlands: Springer Netherlands. doi: 10.1007/978-94-007-1086-3_3
 1366 PFISR. (2025). <https://data.amisr.com/database>.
- 1367 Rees, M. H., & Luckey, D. (1974). Auroral electron energy derived from ratio of
 1368 spectroscopic emissions 1. model computations. *Journal of Geophysical Re-*
 1369 *search*, *79*(34), 5181–5186. doi: 10.1029/JA079i034p05181
- 1370 Ritter, P., Lühr, H., & Rauberg, J. (2013, Nov 01). Determining field-aligned cur-
 1371 rents with the swarm constellation mission. *Earth, Planets and Space*, *65*(11),
 1372 1285–1294. doi: 10.5047/eps.2013.09.006
- 1373 Robinson, R. M., Vondrak, R. R., Miller, K., Dabbs, T., & Hardy, D. (1987). On
 1374 calculating ionospheric conductances from the flux and energy of precipitating
 1375 electrons. *Journal of Geophysical Research: Space Physics*, *92*(A3), 2565–2569.
 1376 doi: 10.1029/JA092iA03p02565
- 1377 Rönmark, K. (2002). Auroral current-voltage relation. *Journal of Geophysical Re-*
 1378 *search: Space Physics*, *107*(A12). doi: 10.1029/2002JA009294
- 1379 Seyler, C. E. (1990). A mathematical model of the structure and evolution of small-
 1380 scale discrete auroral arcs. *Journal of Geophysical Research: Space Physics*,
 1381 *95*(A10), 17199–17215. doi: 10.1029/JA095iA10p17199
- 1382 Solomon, S. C. (2017). Global modeling of thermospheric airglow in the far ultravi-
 1383 olet. *Journal of Geophysical Research: Space Physics*, *122*(7), 7834–7848. doi:
 1384 10.1002/2017JA024314
- 1385 Strickland, D. J., Meier, R. R., Hecht, J. H., & Christensen, A. B. (1989). Deducing
 1386 composition and incident electron spectra from ground-based auroral optical
 1387 measurements: Theory and model results. *Journal of Geophysical Research:*
 1388 *Space Physics*, *94*(A10), 13527–13539. doi: 10.1029/JA094iA10p13527
- 1389 SuperDARN. (2025). <https://superdarn.ca/data-download>.
- 1390 SuperDARN Data Visualization Working Group, Martin, C. J., Rohel, R. A., Bil-
 1391 lett, D. D., Pitzer, P., Galeshuck, D., ... Schmidt, M. T. (2025). [https://](https://zenodo.org/records/14796490)
 1392 zenodo.org/records/14796490.
- 1393 Swarm. (2025). <https://earth.esa.int/eogateway/missions/swarm/data>.
- 1394 van Irsel, J. (2025). <https://rcweb.dartmouth.edu/LynchK/Gemini3D>.
- 1395 van Irsel, J. (2025). https://github.com/317Lab/aurora_gemini.
- 1396 van Irsel, J., Lynch, K. A., Mule, A., & Zettergren, M. D. (2024). Generation of top-
 1397 boundary conditions for 3D ionospheric models constrained by auroral imagery
 1398 and plasma flow data. *Journal of Geophysical Research: Space Physics*, *129*(8),
 1399 e2024JA032722. doi: 10.1029/2024JA032722
- 1400 Wang, X., Cai, L., Aikio, A., Vanhamäki, H., Virtanen, I., Zhang, Y., ... Liu, S.
 1401 (2024). Ionospheric conductances due to electron and ion precipitations: A
 1402 comparison between EISCAT and DMSP estimates. *Journal of Geophysical*
 1403 *Research: Space Physics*, *129*(2). doi: 10.1029/2023JA032354
- 1404 Wolf, R. A. (1975, 01). Ionosphere-magnetosphere coupling. *Space Science Reviews*,
 1405 *17*(2), 537–562. doi: 10.1007/BF00718584
- 1406 Yano, Y., & Ebihara, Y. (2021). Three-dimensional closure of field-aligned cur-
 1407 rents in the polar ionosphere. *Journal of Geophysical Research: Space Physics*,
 1408 *126*(9). doi: 10.1029/2021JA029421
- 1409 Zettergren, M., & Snively, J. (2019). Latitude and longitude dependence of iono-
 1410 spheric TEC and magnetic perturbations from infrasonic-acoustic waves gener-
 1411 ated by strong seismic events. *Geophysical Research Letters*, *46*(3), 1131–1140.
 1412 doi: 10.1029/2018GL081569
- 1413 Zettergren, M. D., & Semeter, J. L. (2012). Ionospheric plasma transport and loss
 1414 in auroral downward current regions. *Journal of Geophysical Research: Space*
 1415 *Physics*, *117*(A6). doi: 10.1029/2012JA017637
- 1416 Zettergren, M. D., & Snively, J. B. (2015). Ionospheric response to infrasonic-
 1417 acoustic waves generated by natural hazard events. *Journal of Geophysical*
 1418 *Research: Space Physics*, *120*(9), 8001–8024. doi: 10.1002/2015JA021116